A Structurally Coupled Disturbance Analysis Method Using Dynamic Mass Measurement Techniques, with Application to Spacecraft-Reaction Wheel Systems

by

Laila Mireille Elias

B.S. Aeronautics and Astronautics
University of Washington, 1998

Submitted to the Department of Aeronautics and Astronautics
in partial fulfillment of the requirements for the degree of

MASTER OF SCIENCE IN AERONAUTICS AND ASTRONAUTICS

at the

MASSACHUSETTS INSTITUTE OF TECHNOLOGY

March 2001

Signature of Author .....
Department of Aeronautics and Astronautics
March 13, 2001

Certified by .....
David W. Miller
Associate Professor
Thesis Supervisor

Accepted by .....
Wallace E. Vander Velde
Professor of Aeronautics and Astronautics
Chairman, Department Graduate Committee

A Structurally Coupled Disturbance Analysis Method Using Dynamic Mass Measurement Techniques, With Application to Spacecraft-Reaction Wheel Systems

by

Laila Mireille Elias

Submitted to the Department of Aeronautics and Astronautics
on March 13, 2001, in Partial Fulfillment of the
Requirements for the Degree of Master of Science
In Aeronautics and Astronautics

ABSTRACT

The next generation of spaceborne telescopes, including NASA's Space Interferometry Mission and Next Generation Space Telescope, are being designed to replace and improve upon the Hubble Space Telescope. A common trait of these space observatories, which aim to have maximum aperture size with minimal weight, is that they are lightweight, flexible structures whose dynamic characteristics can strongly influence their ability to achieve scientific goals. The largest vibrational disturbance source onboard most space observatories is the reaction wheel assembly (RWA), a spinning disk used for attitude control and pointing at scientific targets. RWA-induced vibrational disturbances have often been measured and characterized; the measured disturbances are typically combined with information from a finite element model of the spacecraft before it is launched in order to predict the spacecraft's resulting dynamic behavior. This *traditional disturbance analysis method* is flawed in one main aspect: the RWA disturbances are measured in isolation and do not account for the structural dynamic coupling effects between the RWA and the spacecraft to which it will eventually be mounted.

This thesis suggests a new *coupled disturbance analysis method* that accounts for spacecraft-RWA structural dynamic coupling effects by including two additional terms, the dynamic mass transfer function matrices of the spacecraft and the RWA, in the analysis equations. Both experimental and model-based methods for obtaining all the terms necessary for a coupled analysis are clearly outlined. Experiments performed to validate this coupled disturbance analysis method are described in detail, and the results are presented. Suggestions are made for eliminating errors that corrupt the results, and recommendations for future work are provided.

Thesis Supervisor: David W. Miller
Title: Associate Professor

ACKNOWLEDGMENTS

Funding for this research was provided by NASA's Jet Propulsion Laboratory under contract #961123 (Modeling and Optimization of Dynamics and Control for the NASA Space Interferometry Mission and the Micro-Precision Interferometer Testbed), with Robert Grogan as Technical and Scientific Officer and Dr. Sanjay Joshi as Contract Monitor, and by the NASA Goddard Space Flight Center under contract NAG 5-7839, with Gary E. Mosier as Technical and Scientific Officer.

I wish to thank Professor David Miller for his guidance and support.

Very special thanks go to my father, Professor Ziad Elias, for his detailed review of this manuscript and his numerous, invaluable suggestions.

I am indebted to Olivier DeWeck and Jeremy Yung for their technical guidance, to Rebecca Masterson for paving the road in this subject, to Scott Uebelhart for accompanying me on a parallel journey of thesis-writing and flight lessons, to Timothy Glenn for providing a template for this thesis, and to Sharon-Leah Brown and Margaret Edwards for their continual support.

Finally, I wish to thank my husband, David Cutler, for being my foundation, offering limitless support, and being so incredibly patient, as well as my mother, Ralda, my sister, Maria, my brother, Paul, and the "rest" of my family, Phil, Barb, Nat, and Andrew Cutler, for all of their encouragement.

TABLE OF CONTENTS

LIST OF FIGURES

LIST OF TABLES

NOMENCLATURE

CSD	Cross Spectral Density [N^2/Hz]
DAQ	Data Acquisition System
DOF	Degree of Freedom
FEM	Finite Element Model
HST	Hubble Space Telescope
MIT	Massachusetts Institute of Technology
NGST	Next Generation Space Telescope
PSD	Power Spectral Density [N^2/Hz]
RMS	Root Mean Square
RPM	Revolutions per Minute
RWA	Reaction Wheel Assembly
SNR	Signal-to-Noise Ratio
SIM	Space Interferometry Mission

Chapter 1

INTRODUCTION

Modern-day space-based telescopes pose a new level of design challenge to structural dynamicists and control engineers. They involve two opposing requirements: the first is that the aperture of the telescope be large enough to observe the intended science targets, such as distant stars and planets. The second is that the telescope mass and volume be within the constraints of a given launch vehicle. The result of these two requirements is that space telescopes are generally large, lightweight, flexible, and often deployable structures. The Hubble Space Telescope, for instance, launched in 1990 as the first major infrared-optical-ultraviolet spaceborne telescope, is 13.3 meters long with 5.3 meter lightweight supporting truss structure [STSCI].

A likely future for space telescopes lies with interferometry, which, rather than utilizing one large aperture to collect light, combines light from multiple, smaller apertures spread at a large distance from one another. Hence the quality of interferometric observation depends not on the *size* of a monolithic aperture, but on the *distance* between multiple apertures. For this reason, future space interferometers, such as NASA's forthcoming Space Interferometry Mission, are larger and more flexible than ever. Further, their ability to precisely interfere light from multiple apertures depends greatly on the vibratory behavior of the structure. For this reason, strict tolerances are placed on the magnitudes and frequencies of vibration of such spacecraft, and detailed disturbance analyses and control

design are required to ensure that deflections and vibrations are limited to acceptable levels for scientific observation.

Reaction Wheel Assemblies (RWAs), which are used for attitude control aboard many spacecraft and are proposed for use on future space telescopes such as NASA's forthcoming Space Interferometry Mission, are never manufactured perfectly, and induce certain disturbances while spinning. Although disturbances can also be induced by on-board equipment such as tape recorders or centrifuges, RWAs are anticipated to be the largest vibrational disturbance source aboard future space telescopes, so various methods have been developed to characterize and measure their disturbances and to use these measurements to predict the spacecraft's resulting dynamic behavior.

1.1 Reaction Wheel Applications

Reaction wheel assemblies have been used for attitude control aboard numerous spacecraft to date, including the Hubble Space Telescope, and are anticipated for use in future scientific missions, such as NASA's Space Interferometry Mission (SIM) and Next Generation Space Telescope (NGST), which are both elements of NASA's Origins Program.

The Origins Program, which consists of several closely-spaced missions over the next two decades, was created by NASA to study the origins of our universe. It will investigate everything from the birth of distant galaxies to the characteristics of nearby stars, some of which may harbor Earth-like planets capable of sustaining life. This program seeks to answer fundamental questions about the development of the universe and the possibility that life may exist beyond Earth. SIM and NGST are two of several space-based observatories that comprise the Origins Program.

The Space Interferometry Mission, depicted in Figure 1.1, is scheduled for launch in 2006, and will be the first spacecraft to demonstrate optical interferometry. SIM will combine light collected from seven apertures spread along its ten-meter flexible support structure to form three optical interferometers. With optical requirements translating to positional sta-

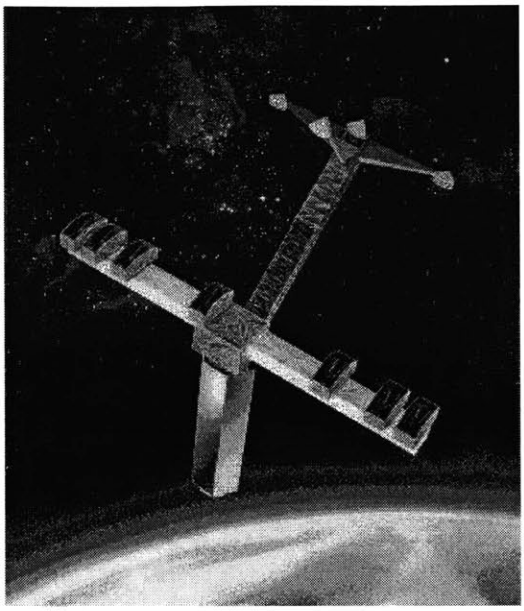

Figure 1.1 Proposed Design for NASA's Space Interferometry Mission (SIM) [NASA]

bility tolerances on the order of nanometers, the structural dynamics of this flexible spacecraft are of great concern, especially in the presence of vibrational disturbance sources such as spinning reaction wheels. Detailed analyses have already demonstrated that the positional stability requirements would not be met with Hubble-quality reaction wheels, which induce smaller disturbances than any other wheels flown to date [Uebelhart, 2001].

The Next Generation Space Telescope, depicted in Figure 1.2, is the follow-up mission to the Hubble Space Telescope, and is scheduled to launch in 2009. Like SIM, NGST will study the origins of the universe by observing distant stars, galaxies, and earth-like planets. NGST will provide views of reaches of the universe never observed before.

NGST is a large, flexible structure with an ~8 meter diameter primary mirror. Like SIM, NGST will depend on reaction wheels for attitude control and precision pointing at targets. Hence the ability of NGST to successfully accomplish scientific goals will also depend greatly on the magnitude of its reaction wheel disturbances.

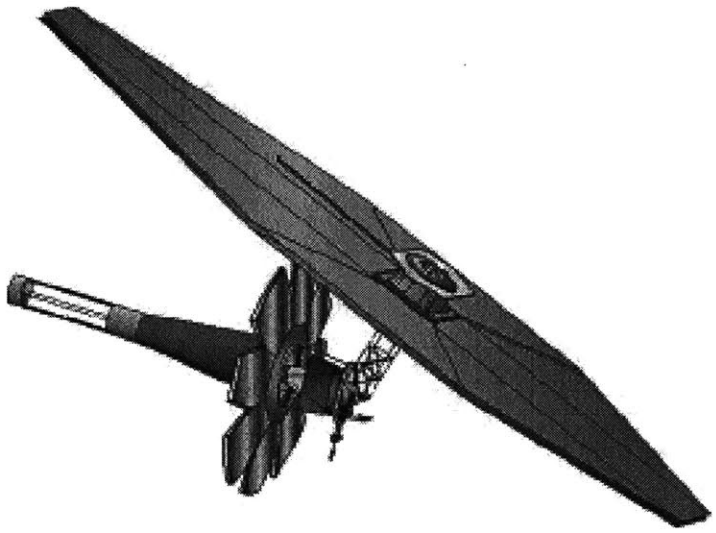

Figure 1.2 Proposed Design for NASA's Next Generation Space Telescope (NGST) [NASA]

1.2 Reaction Wheels for Attitude Control

Reaction wheels are momentum exchange devices that control a spacecraft's attitude by "exchanging" momentum with the spacecraft. They operate on the principle of *conservation of angular momentum* of a closed system; by accelerating about one axis, reaction wheels force a spacecraft to rotate in the opposite direction about the same axis, thus conserving the total angular momentum of the system. Reaction wheels are used in this manner to orient spacecraft for scientific observation and data collection and to counterbalance small external disturbance torques caused by factors such as residual atmospheric drag, gravity gradients, and interaction with the earth's magnetic field.

Figure 1.3(a) shows the exterior view of an Ithaco Type E reaction wheel assembly, and Figure 1.3(b) shows the corresponding cross-sectional view. The primary components include the housing, shown in Figure 1.3(a), and the flywheel and electric motor, depicted in Figure 1.3(b). By producing a variable torque, the motor controls the spin rate of the flywheel, causing it to accelerate or decelerate as necessary. Notice that the flywheel's mass is concentrated at the outer edge of its diameter, maximizing its mass moment of inertia about the spin axis and thus its torque authority over the spacecraft.

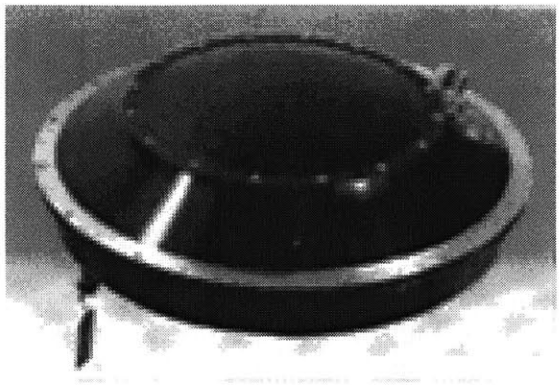

(a)

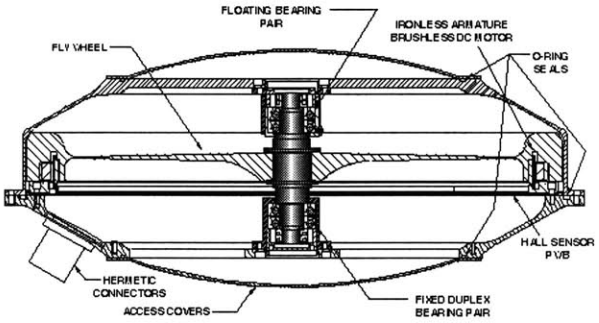

(b)

Figure 1.3 Ithaco Type E Reaction Wheel: (a) Exterior Photograph and (b) Cross-Sectional View [Ithaco]

1.3 Thesis Overview

Because RWAs may induce detrimental vibrational disturbances on-board future precision space structures, their disturbances must be carefully measured and characterized during the mission design phase; a *disturbance analysis* can then be performed on the structure, whereby measured wheel disturbance data are combined with outputs from a spacecraft structural model in order to predict the structure's resulting dynamic behavior. For an optical interferometer such as SIM, the structural dynamics can then be mapped to optical performance metrics in order to assess whether the wheel disturbances will inhibit the spacecraft's ability to achieve scientific goals.

This thesis presents the usual method of disturbance analysis and investigates an approximation made in this method that neglects the effect of structural dynamic coupling

between the flexible space structure and its disturbance-inducing reaction wheel. An amended *coupled disturbance analysis* method is then presented and validated using representative hardware.

An organizational overview of this thesis is shown in Figure 1.4. Background information

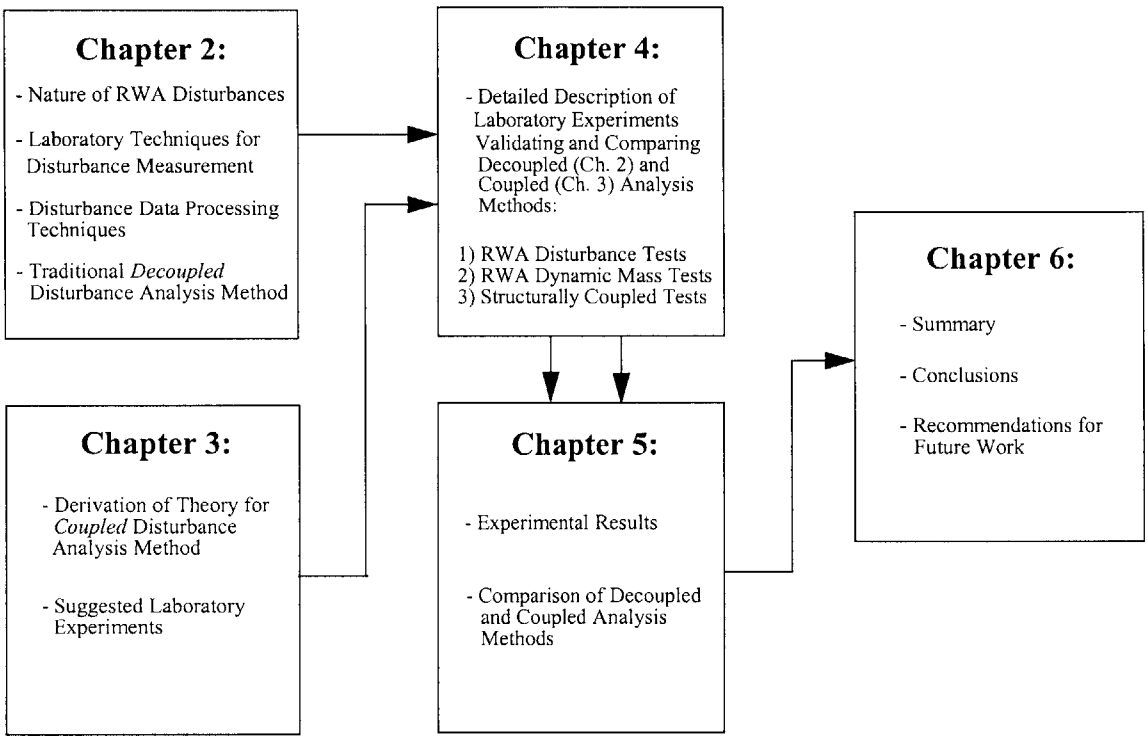

Figure 1.4 Thesis Overview

on the nature of reaction wheel vibrational disturbances and the usual method of measuring and characterizing them is presented in Chapter 2, along with the traditional *decoupled* disturbance analysis method.

In Chapter 3, the theory for the new disturbance analysis method that *accounts for the structural dynamic coupling between a flexible body and its disturbance source* is introduced. Laboratory experiments are then recommended to validate this method.

In Chapter 4, the hardware and experimental configurations used to validate the decoupled and coupled disturbance analysis methods are described in detail. The experimental results are presented in Chapter 5 with a comparison of the two methods, and finally a summary, conclusions, and recommendations for future work are presented in Chapter 6.

Chapter 2

REACTION WHEEL DISTURBANCE TESTING

While playing a vital role in the attitude control of most spacecraft, reaction wheels are anticipated to cause the largest on-board vibrational disturbances. This is of especially great concern for large, flexible spacecraft, and specifically for spaceborne telescopes and interferometers that have extremely precise positional and vibratory tolerances imposed on them in order to achieve scientific goals.

In order to predict the effect of reaction wheel assembly (RWA) disturbances on future spacecraft being designed or built, it is necessary to understand and characterize the reaction wheels and the disturbances they induce.

The nature of RWA disturbances is discussed in Section 2.1, followed by a commonly accepted method of measuring the disturbances in Section 2.2. Then the traditional method of applying the measured disturbances to a spacecraft model in order to predict the spacecraft's behavior is introduced in Section 2.3. Finally, a summary of this chapter is presented in Section 2.4.

2.1 Nature of Reaction Wheel Disturbances

Reaction wheel disturbances are generally sinusoidal and tonal in nature, occurring at a set of distinct frequencies. Generally the most significant disturbance, known as the *primary*

harmonic of the RWA, occurs at the same frequency as the wheel's spin rate, and is caused by imbalances of the flywheel due to manufacturing imperfections.

Flywheel imbalance is generally characterized by the sum of a *static imbalance* and a *dynamic imbalance*. Static imbalance occurs when the wheel's center of gravity is misaligned with the spin axis. This is best visualized as a small lumped mass m attached to an otherwise perfectly balanced, axially symmetric flywheel, as shown in Figure 2.1. The

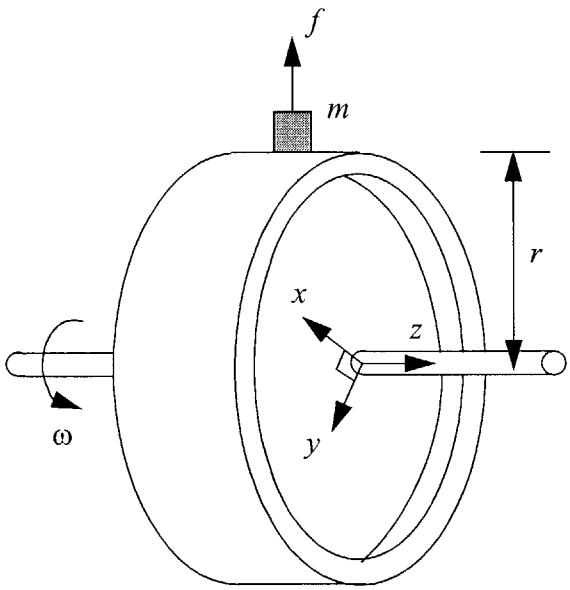

Figure 2.1 Static Imbalance of a Flywheel

resulting disturbance is a radial force exerted on the wheel, caused by the centripetal force acting on the spinning imbalance. The magnitude of this force is:

$$f = mr\omega^2, \tag{2.1}$$

where r is the imbalance radius and ω is the wheel's spin rate. Because the imbalance is fixed to the rotating frame of the wheel, the force appears sinusoidal in a fixed reference frame. For example, if the orthogonal xyz coordinate system shown in Figure 2.1 is fixed in the inertial frame, with the x and y axes in the plane of the flywheel and the z axis

aligned with the flywheel's spin axis, then the disturbance forces f_x and f_y occurring along the x and y axes, respectively, are sinusoidal in time with frequency equal to the wheel's spin rate, ω, and are separated from each other in phase by 90 degrees.

The dynamic imbalance is caused by angular misalignment of the wheel's principal inertia axis with its spin axis. This can be visualized as two lumped masses placed opposite each other radially and at an offset from each other axially by a distance d, as shown in Figure 2.2. The resulting disturbance occurs at the wheel's spin rate and induces a cou-

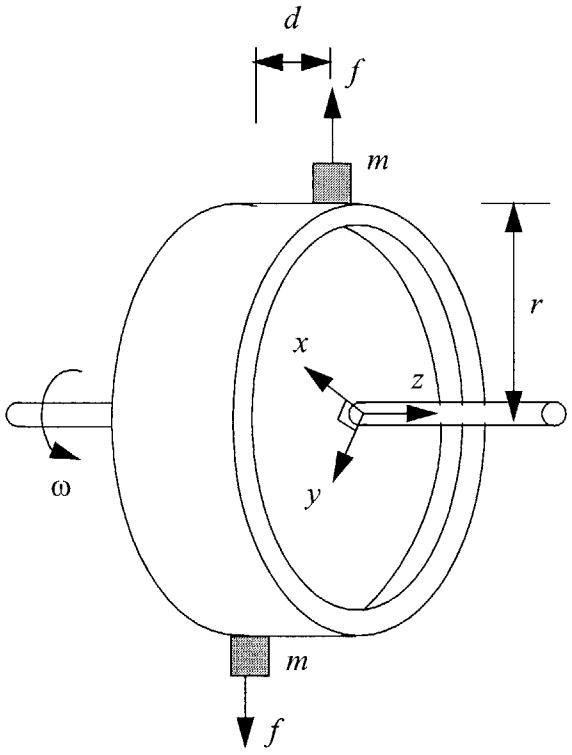

Figure 2.2 Dynamic Imbalance of a Flywheel

pling moment on the wheel with magnitude:

$$M = mrd\omega^2 \tag{2.2}$$

Just like the force caused by a static imbalance, the moment caused by a dynamic imbalance appears sinusoidal from a fixed reference frame.

The *superharmonics* and *subharmonics* of a RWA are tonal disturbances occurring at multiples and fractions of the wheel spin rate, respectively. These disturbances are often attributed to bearing disturbances, motor disturbances, and motor driver errors [Bialke, 1997].

A third contributor to reaction wheel-induced disturbances is the flexibility of the wheel itself. The wheel can be modeled as a one-degree-of-freedom (DOF) system in the axial direction and a 2-DOF system in the radial direction, yielding three dominant flexible modes: the axial translation mode, the radial translation mode, and the radial rocking mode, all demonstrated in Figure 2.3 [Bialke, 1997].

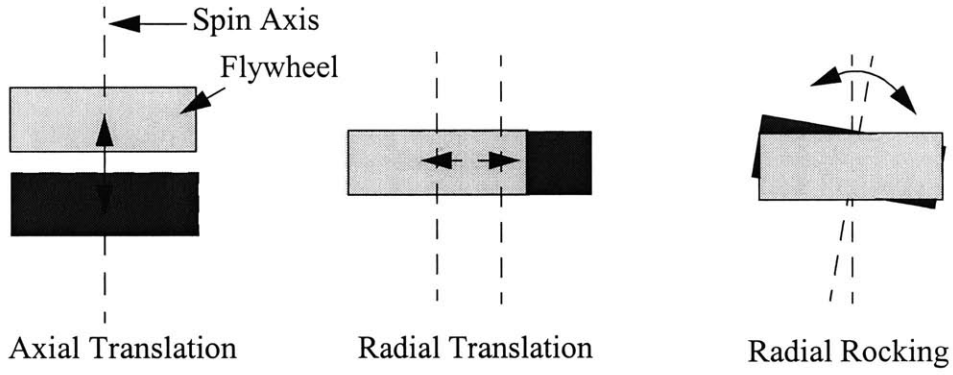

Figure 2.3 Three Dominant Vibrational Modes of a Reaction Wheel

When a wheel's spin rate induces harmonics at the same frequency as a structural mode of the wheel, large amplifications to the harmonic disturbances occur. This is discussed further in Chapter 5, where some measured disturbance data showing this phenomenon are presented.

2.2 Current Disturbance Testing Techniques

In this section, the primary method of measuring reaction wheel disturbances is presented, along with techniques for processing the disturbance data and using it to predict a spacecraft's resulting dynamic behavior.

2.2.1 Hard-Mounted Testing

Hard-mounted testing is the most common method of characterizing reaction wheel disturbances. In this method, the RWA is mounted to a rigid surface and spun at various speeds. The resulting disturbances are then measured and eventually used to predict the vibrational response of the structure to which the wheel will be mounted.

The RWA is first fixed to the top face of a load transducer, which measures the relative forces and moments across its two faces. The bottom face of the transducer is then fixed to a rigid surface, as shown in Figure 2.4. Hence the transducer measures disturbances

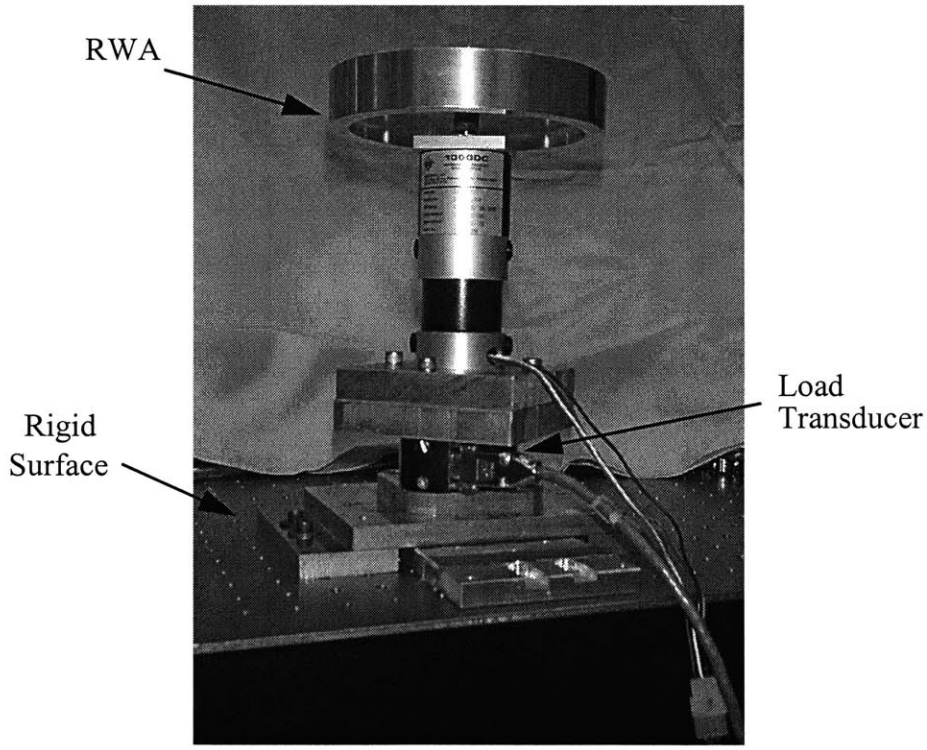

Figure 2.4 Typical Hard-Mounted RWA Testing Configuration

caused by the spinning wheel with *fixed* boundary conditions, since the wheel's interface at the transducer is constrained to have zero motion.

The wheel can either be spun at a set of distinct speeds, or it can be swept continuously through a range of speeds. In either case, the RWA disturbances are measured by the load transducer as forces along three axes and moments about three axes. These disturbance loads are generally recorded in the time domain and then processed to obtain useful frequency domain data. This data processing is described in the next section.

2.2.2 Data Processing Techniques

The three disturbance forces and three disturbance moments measured by a six-axis load transducer in hard-mounted RWA tests are generally recorded as voltage time histories. These time histories are converted to physical units using a calibration factor specific to the load transducer, and are then processed in both the time and frequency domains.

Time Domain Techniques

In the time domain, the *expected value* of a signal *f(t)* is the same as the signal's *mean* value, $\mu_f(t)$:

$$\mu_f(t) = E[f(t)] \tag{2.3}$$

where $E[\cdot]$ is the expectation operator. The *variance*, $\sigma_f^2(t)$, of the signal is then:

$$\sigma_f^2(t) = E[\{f(t) - \mu_f(t)\}^2] \tag{2.4}$$

and its square root, $\sigma_f(t)$, is known as the *standard deviation*.

The *mean square*, $r_f^2(t)$, is the expected value of the square of the signal:

$$r_f^2(t) = E[f(t)^2] \tag{2.5}$$

and the *root mean square* (RMS), $r_f(t)$, is the square root of this value.

With these definitions, it is important to notice that for a zero-mean signal, with $\mu_f = 0$, the variance and the mean square are equal, and hence the standard deviation and the RMS are equal.

Finally, the *autocorrelation function*, which measures the correlation of a signal $f(t)$ with itself at two different times, is defined as:

$$R_f(t_1, t_2) = E[f(t_1)f(t_2)] \tag{2.6}$$

and the *cross-correlation function*, which measures the correlation between two different signals $f_x(t)$ and $f_y(t)$, is defined as:

$$R_{f_x f_y}(t_1, t_2) = E[f_x(t_1)f_y(t_2)] \tag{2.7}$$

A *weakly stationary process* is one whose mean and variance are constant with time and whose autocorrelation and cross-correlation functions depend only on the *difference* τ between times t_1 and t_2, so that:

$$R_f(\tau) = R_f(t, t+\tau) = E[f(t)f(t+\tau)] \tag{2.8}$$

and

$$R_{f_x f_y}(\tau) = R_{f_x f_y}(t, t+\tau) = E[f_x(t)f_y(t+\tau)] \tag{2.9}$$

All the signals in this thesis are considered weakly stationary, zero-mean sinusoidal disturbances, so the auto- and cross-correlation functions will be written as Equations 2.8 and 2.9, the variance will be considered constant, and the RMS and standard deviation will be used interchangeably.

Frequency Domain Techniques

The Fourier transform is a well-known method of decomposing time signals into their frequency content. The *forward Fourier transform* of a time domain signal, $f(t)$, is defined as:

$$F(\omega) = \frac{1}{2\pi}\int_{-\infty}^{\infty} f(t)e^{-i\omega t}dt \tag{2.10}$$

where $F(\omega)$ is complex. The *inverse Fourier transform*, which yields a time history from a Fourier signal, is:

$$f(t) = \int_{-\infty}^{\infty} F(\omega) e^{i\omega t} d\omega \tag{2.11}$$

Note that the $\frac{1}{2\pi}$ factor in the Fourier transform definition is often omitted from Equation 2.10 and included instead in inverse Fourier transform definition in Equation 2.11. Either method is fine, so long as the two definitions are consistent with each other.

A limitation of Equation 2.10 is that it integrates over infinite time, and thus does not hold for stationary signals, since they are not absolutely integrable [Wirsching, 1995]. Further, it is impossible to actually measure an infinitely-long signal *f(t)*. In this case, it is useful to define the *finite Fourier transform* of *f(t)* over the interval $(0,T)$ as:

$$F(\omega, T) = \int_{0}^{T} f(t) e^{-i\omega t} dt \tag{2.12}$$

This differs from Equation 2.10 in both the finite integration limits and the absence of a $\frac{1}{2\pi}$ factor.

Notice that the magnitude of the finite Fourier transform in Equation 2.12 is dependent on the length T of the time history being integrated. To estimate the amplitude of the signal *f(t)* as a function of frequency, the finite Fourier transform can be normalized by T to obtain the *amplitude spectrum* of the signal:

$$A_F(\omega) = \frac{1}{2\pi T} \left| \int_{0}^{T} f(t) e^{-i\omega t} dt \right| \tag{2.13}$$

where we have accounted for the $\frac{1}{2\pi}$ factor lost in the step from the forward to the finite Fourier transform. Unlike the Fourier transform, the amplitude spectrum is a real-valued function.

We now define the *power spectral density function* (PSD) of a time signal, which is a frequency domain variable often employed in disturbance analyses. The PSD, $\phi_F(\omega)$, of a signal *f(t)* has two equivalent definitions. The first is based directly on the time history of the signal, and is defined as the Fourier transform of the signal's autocorrelation function:

$$\phi_F(\omega) = \frac{1}{2\pi}\int_{-\infty}^{\infty} R_f(\tau)e^{-i\omega\tau}d\tau \tag{2.14}$$

where the autocorrelation function can be recovered from the PSD as:

$$R_f(\tau) = \int_{-\infty}^{\infty} \phi_F(\omega)e^{i\omega\tau}d\omega \tag{2.15}$$

The second is perhaps a more useful definition for signal processing purposes, and is based upon the finite Fourier transform of the signal:

$$\boxed{\phi_F(\omega) = \lim_{T\to\infty}\frac{1}{2\pi T}E[|F(\omega, T)|^2]} \tag{2.16}$$

[Wirsching, 1995] has shown that these two definitions are equivalent.

Similarly, the *cross spectral density function* (CSD) of two time signals, $f_x(t)$ and $f_y(t)$, is defined first as:

$$\phi_{F_xF_y}(\omega) = \frac{1}{2\pi}\int_{-\infty}^{\infty} R_{F_xF_y}(\tau)e^{-i\omega\tau}d\tau \tag{2.17}$$

where the cross-correlation function can be recovered from the CSD as:

$$R_{F_xF_y}(\tau) = \int_{-\infty}^{\infty} \phi_{F_xF_y}(\omega)e^{i\omega\tau}d\omega \tag{2.18}$$

and second as:

$$\phi_{F_xF_y}(\omega) = \lim_{T\to\infty} \frac{1}{2\pi T} E[F_x(\omega, T)F_y(\omega, T)] \tag{2.19}$$

Again, the latter definition is often more practical. Note that while the power spectral density is a real-valued function, the cross-spectral density is complex and *Hermitian*, so that:

$$\phi_{F_xF_y}(\omega) = \phi_{F_yF_x}{}^*(\omega) \tag{2.20}$$

where $[\,\cdot\,]^*$ denotes a complex conjugate value. Often the power and cross spectral densities of a set of signals are grouped together in a *spectral density matrix*, Φ, where each diagonal entry is the PSD of a signal, and each off-diagonal entry is the CSD between two signals. For instance, the six-axis set of disturbances obtained in a hard-mounted RWA test can be placed in a 6×6 spectral density matrix, $\Phi_{FF}(\omega)$, where the six diagonal entries are PSDs of the six disturbance signals, and the off-diagonal entries are the corresponding CSDs between disturbance signals:

$$F(\omega) = \begin{Bmatrix} F_x \\ F_y \\ F_z \\ M_x \\ M_y \\ M_z \end{Bmatrix}, \quad \Phi_{FF}(\omega) = \begin{bmatrix} \phi_{F_x} & \phi_{F_xF_y} & \phi_{F_xF_z} & \phi_{F_xM_x} & \phi_{F_xM_y} & \phi_{F_xM_z} \\ \phi_{F_yF_x} & \phi_{F_y} & \phi_{F_yF_z} & \phi_{F_yM_x} & \phi_{F_yM_y} & \phi_{F_yM_z} \\ \phi_{F_zF_x} & \phi_{F_zF_y} & \phi_{F_z} & \phi_{F_zM_x} & \phi_{F_zM_y} & \phi_{F_zM_z} \\ \phi_{M_xF_x} & \phi_{M_xF_y} & \phi_{M_xF_z} & \phi_{M_x} & \phi_{M_xM_y} & \phi_{M_xM_z} \\ \phi_{M_yF_x} & \phi_{M_yF_y} & \phi_{M_yF_z} & \phi_{M_yM_x} & \phi_{M_y} & \phi_{M_yM_z} \\ \phi_{M_zF_x} & \phi_{M_zF_y} & \phi_{M_zF_z} & \phi_{M_zM_x} & \phi_{M_zM_y} & \phi_{M_z} \end{bmatrix} \tag{2.21}$$

From Equation 2.20, we know that this spectral density matrix is Hermitian:

$$\Phi_{FF}(\omega) = \Phi_{FF}^H(\omega) = \Phi_{FF}^{T\,*}(\omega) \tag{2.22}$$

In other words, Φ_{FF} is equal to its Hermitian value, or its complex conjugate transpose.

With these definitions, we can now write a relation between the RMS and the PSD of a stationary, zero-mean signal. Combining Equations 2.4, 2.8, and 2.15 yields:

$$\sigma_f^2 = E[f(t)^2] = R_f(\tau = 0) = \int_{-\infty}^{\infty} \phi_F(\omega) e^{i\omega 0} d\omega = \int_{-\infty}^{\infty} \phi_F(\omega) d\omega \tag{2.23}$$

so that the RMS, r_f, equivalent to the standard deviation, σ_f, of a zero-mean signal $f(t)$, can be written as the square root of the integrated PSD function:

$$r_f = \left[\int_{-\infty}^{\infty} \phi_F(\omega) d\omega \right]^{\frac{1}{2}} \tag{2.24}$$

Hence for any stationary, zero-mean signal, the RMS can be computed as the square root of the area under the PSD curve.

A useful extension of this result is the *cumulative RMS function*:

$$r_f^{cum}(\omega) = 2\left[\int_0^{\omega} \phi_F(\tilde{\omega}) d\tilde{\omega} \right]^{\frac{1}{2}} \tag{2.25}$$

where the factor of 2 arises from the fact that we have shifted from a two-sided integration in Equation 2.24 to a one-sided integration in 2.25. Notice that for infinitely large frequencies, the cumulative RMS recovers the total RMS of a signal:

$$\lim_{\omega \to \infty} r_f^{cum}(\omega) = r_f \tag{2.26}$$

The cumulative RMS function represents a cumulative contribution to the total RMS of a signal as a function of frequency. Since the cumulative RMS "integrates" a PSD along the frequency axis, large steps in its value occur at frequencies where $\phi_F(\omega)$ "spikes" to large

values. Hence the cumulative RMS is a useful tool in structural dynamic applications because it allows one to visualize the frequencies of vibrational modes that contribute most to the RMS of a vibratory response.

Figure 2.5 shows the PSD of a typical reaction wheel disturbance force, along with its cumulative RMS function. The PSD, $\phi_{F_x}(\omega)$, represents the power density of a wheel's

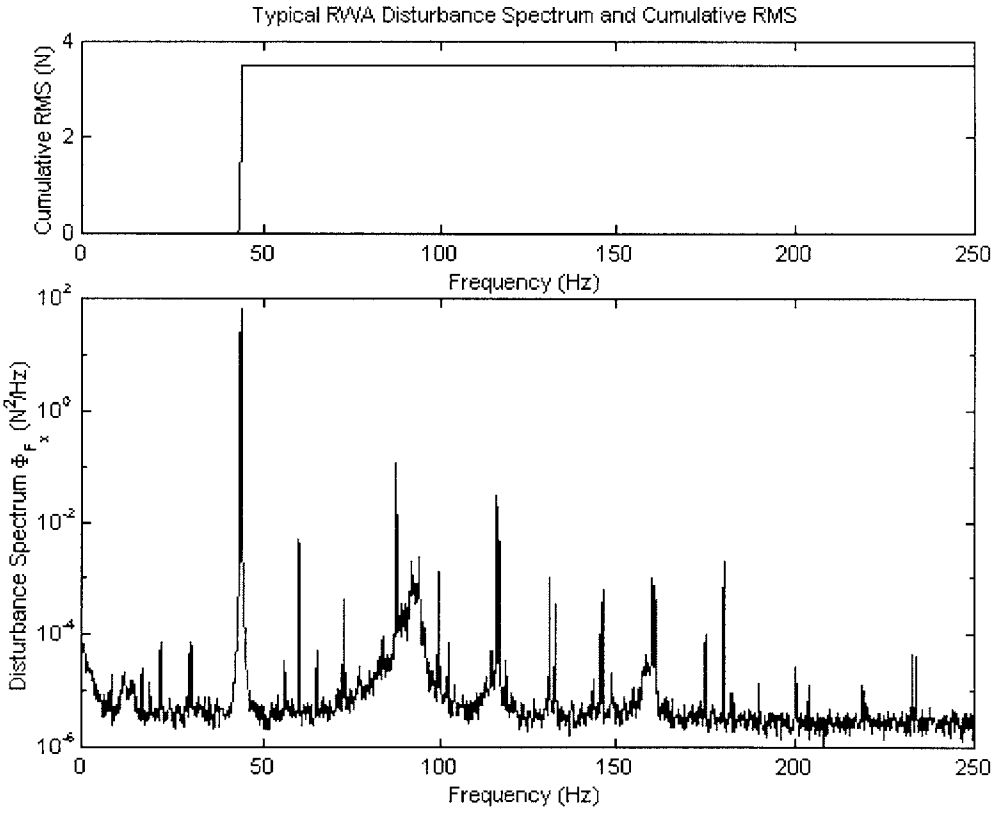

Figure 2.5 Typical Reaction Wheel Disturbance Spectrum and Cumulative RMS Function

x-axis disturbance force as a function of frequency. The largest spike occurs at 44 Hz, representing the primary harmonic. This spike in $\phi_{F_x}(\omega)$ maps to a large step in the cumulative RMS function at the same frequency, indicating a significant contribution to the energy of the disturbance signal. This technique of identifying key disturbance fre-

quencies from steps in the cumulative RMS function is an important result that will be employed throughout this thesis.

It is important to remember that the fidelity of all these frequency domain variables is dependent, in the end, on the quality of data acquisition in the time domain. The key rule in this matter is that the digital sampling frequency must be greater than twice the bandwidth of interest, known as the Nyquist or "folding" frequency, in order to avoid aliasing of the data. Thus if the desired bandwidth is 500 Hz, the data must be sampled at a frequency greater than $f_s = 1000$ Hz, or a time step smaller than $\Delta t = 10^{-3}$ s.

2.3 Disturbance Analysis Methodology

After obtaining the disturbance spectral density matrix, Φ_{FF}, from RWA hard-mounted tests as described in Section 2.2, one can use these measurements to predict the dynamic behavior of the structure that will eventually be coupled with the wheel. Generally, the structure is not readily available, so an accurate finite element model of the structure is created and used to represent the structure's dynamic behavior.

The structure's dynamic behavior is generally expressed in the form of a transfer function, G_{YF}, relating the disturbance inputs, F, on the structure to the measured outputs, Y. In the case of a structure coupled with a spinning reaction wheel, the disturbance inputs, F, are three disturbance forces and three disturbance moments, as described in Section 2.2. When measured outputs can be mapped algebraically or via integration or differentiation to performance metrics of interest, Z, the transfer function may be expressed as G_{ZF}, relating disturbance inputs to performance metrics.

A common method in frequency domain disturbance analysis, which will be derived in Chapter 3, relates the spectral densities of the disturbances and performance metrics as:

$$\Phi_{ZZ}(\omega) = G_{ZF}(\omega)\Phi_{FF}(\omega)G_{ZF}^{H}(\omega) \tag{2.27}$$

where $[\cdot]^{H}$ denotes a Hermitian value, as defined by Equation 2.22. Hence by obtaining the RWA disturbance spectral density matrix, $\Phi_{FF}(\omega)$, from hard-mounted tests and the structure's disturbance-to-performance transfer function, $G_{ZF}(\omega)$, from an accurate finite element model (FEM), one can predict the spectral density matrix of the performance metrics of the structure using Equation 2.27. This method is the basis for most frequency domain disturbance analyses.

Once the performance metrics are obtained in spectral density matrix form, $\Phi_{ZZ}(\omega)$, the RMS values and cumulative RMS functions of the performance metrics can be calculated by applying the relations derived in Section 2.2.2 to the diagonal elements of the performance spectral density matrix.

The key item to note here is that Equation 2.27, when applied to a spacecraft-RWA system, does not account for the structural dynamic coupling between the spacecraft and the RWA. When the RWA is actually mounted on the spacecraft, its disturbances excite the spacecraft, which in turn excites the wheel, and so forth, producing a dynamic coupling effect between the two bodies. However, the disturbance spectra, $\Phi_{FF}(\omega)$, in Equation 2.27 are obtained from hard-mounted tests of an *isolated* RWA, with *fixed* boundary conditions that do not accurately represent the coupled boundary conditions of the RWA mounted to the spacecraft. These isolated spectra are then propagated directly through the spacecraft transfer function, $G_{ZF}(\omega)$, in Equation 2.27, without accounting for any coupled dynamic effects. The approximation invoked in this *decoupled disturbance analysis method* is the focus of this thesis, and an amended *coupled disturbance analysis method*, which accounts for the structural dynamic coupling between a spacecraft and its RWA, will be introduced in the next chapter.

Finally, note that when Equation 2.27 is applied to a system driven by a unit-intensity white noise disturbance, the performance PSD becomes:

$$\Phi_{ZZ}(\omega) = G_{ZF}(\omega)G_{ZF}^{H}(\omega) \tag{2.28}$$

In this case, the cumulative RMS function, defined in Section 2.2.2, can be calculated by substituting the square of the transfer function $G_{ZF}(\omega)$ in place of the output PSD. This result will be employed in Chapter 3.

2.4 Summary

In this chapter, the nature of RWA disturbances was discussed in Section 2.1, the typical hard-mounted testing method of RWAs was described in Section 2.2, including a discussion of techniques in data processing in the time and frequency domains, and a popular method of spacecraft-RWA frequency domain disturbance analysis was presented in Section 2.3, along with a discussion on the limitations of this method.

In summary, RWA disturbances are composed of a primary harmonic and sub- and super-harmonics of the wheel's spin rate. The dominant flexible modes of a reaction wheel are the axial translation, radial translation, and radial rocking modes. The disturbances are usually measured in six-axes, as three forces and three moments, in a hard-mounted configuration. Data processing techniques are used to convert the six load time histories to useful data, including the 6×6 spectral density matrix, $\Phi_{FF}(\omega)$. A frequency domain disturbance analysis method then combines this disturbance matrix $\Phi_{FF}(\omega)$ with a structural transfer function, $G_{ZF}(\omega)$, obtained from a finite element model of the structure, to predict the resulting performance metrics using Equation 2.27. Tools such as the RMS and cumulative RMS can then be used to assess the performance.

An amended disturbance analysis method, which accounts for the structural dynamic coupling between a spacecraft and RWA, will now be discussed in Chapter 3.

Chapter 3

STRUCTURAL COUPLING THEORY

Traditional testing of reaction wheel assemblies (RWAs) is performed with the wheel hard-mounted to a rigid surface, and isolated from the structure on which it will eventually be mounted. This is necessary because the structure is often a spacecraft in the process of being designed or built, and is generally not available for coupled boundary condition disturbance tests with the wheel.

In this traditional method of RWA disturbance testing, the fixed boundary conditions of the wheel do not accurately represent the eventual boundary conditions of the wheel interfaced with the spacecraft. Since most space-based telescopes that use reaction wheels for attitude control are large, flexible structures, the spacecraft-RWA interface will connect two flexible systems, rather than a flexible and a fixed, rigid system. While the traditional hard-mounted testing method is commonly accepted, this thesis investigates whether it is an accurate approximation, and it derives a method for augmenting the isolated test results in order to account for structural coupling between the spacecraft and RWA.

In Section 3.1, a sample problem is presented to motivate a coupled approach to disturbance analysis. The theory behind the proposed coupled method is then presented in Section 3.2 and applied to a spacecraft-RWA system in Section 3.3. Finally, a summary of the proposed method is presented in Section 3.4.

3.1 Two Degree-Of-Freedom Sample Problem

In order to motivate this structural coupling study, the following two-degree-of-freedom (DOF) sample problem is presented, based on similar work by Masterson [Masterson, 1999]. Consider the two-DOF system shown in Figure 3.1(a), where k_s and m_s represent a simplified one-DOF flexible spacecraft and k_w and m_w represent a one-DOF flexible reaction wheel. This figure represents a coupled spacecraft-RWA system, while Figure 3.1(b) demonstrates a simplified analogy to hard-mounted disturbance testing.

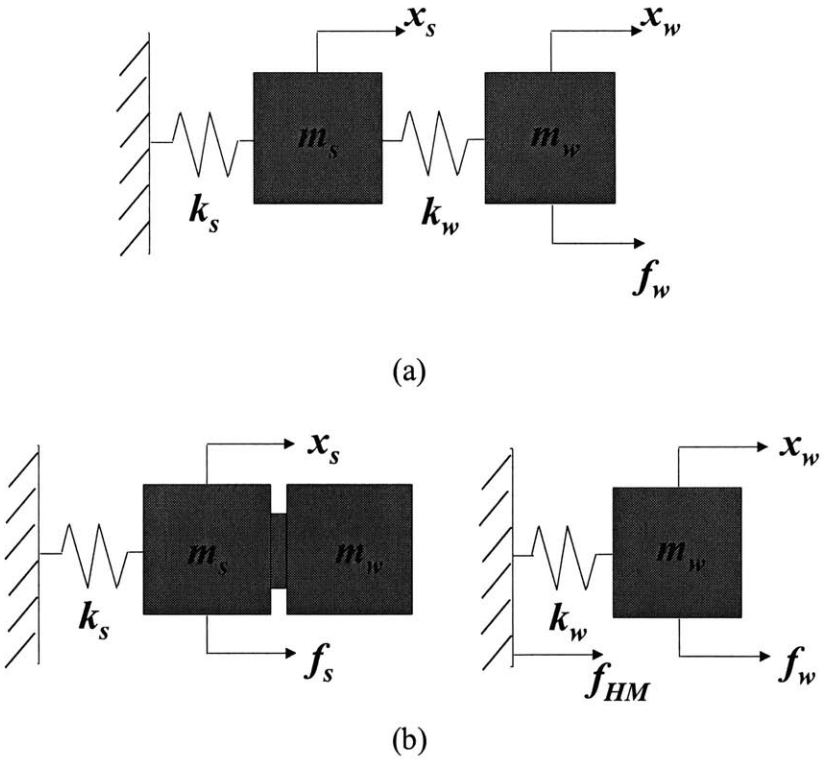

Figure 3.1 (a) Two-DOF Analogy to Coupled Spacecraft-RWA System
(b) Two-DOF Analogy to Decoupled Approximation

In the coupled system analogy shown in Figure 3.1(a), f_w represents the disturbance force imparted on the reaction wheel due to its spinning. This disturbance is propagated through the coupled system to cause displacements x_s and x_w of the spacecraft and RWA, respectively. The performance metric of the system is the spacecraft displacement, x_s.

In the hard-mounted testing analogy shown in Figure 3.1(b), the wheel is represented as a one-DOF spring-mass system fixed to a rigid surface. The same disturbance f_w is applied to the wheel, and the resulting hard-mounted interface force f_{HM} is measured at the fixed end. This interface force, analogous to a multi-DOF set of interface forces (f_x, f_y, and f_z) and moments (m_x, m_y, and m_z) typically measured in hard-mounted RWA disturbance tests, is then applied to the spacecraft model as $f_s = f_{HM}$ in order to predict the resulting performance, x_s. Note that the decoupled spacecraft model includes the mass, m_s, and flexibility, k_s, of the spacecraft, *as well as* the mass, m_w, of the reaction wheel; this follows the method often employed in multi-DOF decoupled disturbance analyses, where the spacecraft finite element model includes the RWA mass and inertia, but doesn't account for its flexibility.

In the *coupled case* shown in Figure 3.1(a), the net force exerted on m_w is:

$$\sum f_{m_w} = f_w - k_w(x_w - x_s) \tag{3.1}$$

so that the wheel's equation of motion is:

$$m_w\ddot{x}_w = \sum f_{m_w} = f_w - k_w(x_w - x_s) \tag{3.2}$$

Taking the Laplace transform of 3.2 and solving for $X_w(s) = \mathcal{L}[x_w(t)]$ yields:

$$X_w = \frac{F_w + k_w X_s}{m_w s^2 + k_w} \tag{3.3}$$

where $X_s(s) = \mathcal{L}[x_s(t)]$, $F_w(s) = \mathcal{L}[f_w(t)]$, and $s = \sigma + j\omega$ is the Laplace variable.

Similarly, the net force exerted on m_s is:

$$\sum f_{m_s} = k_w(x_w - x_s) - k_s x_s \tag{3.4}$$

so that the spacecraft's equation of motion is:

$$m_s\ddot{x}_s = \sum f_{m_s} = k_w(x_w - x_s) - k_s x_s \tag{3.5}$$

Taking the Laplace transform of 3.5 and solving for X_s yields:

$$X_s = \frac{k_w X_w}{m_s s^2 + k_w + k_s} \tag{3.6}$$

If Equation 3.3 is now substituted into 3.6 for X_w:

$$X_s = \frac{k_w(F_w + k_w X_s)}{(m_s s^2 + k_w + k_s)(m_w s^2 + k_w)} \tag{3.7}$$

then Equation 3.7 can be solved for X_s, to yield the coupled input-output relationship between the disturbing force, F_w, applied to the wheel and the spacecraft performance metric, X_s:

$$X_s = G_{X_s F_w} F_w \tag{3.8}$$

where:

$$G_{X_s F_w} = \frac{k_w}{m_w m_s s^4 + [k_w(m_s + m_w) + k_s m_w]s^2 + k_s k_w} \tag{3.9}$$

Coupled Input-Output Relation

A similar analysis can now be performed for the *decoupled case* depicted in 3.1(b). The hard-mounted wheel's equation of motion no longer depends on the relative displacement of the wheel and spacecraft, but rather on the absolute displacement of the wheel:

$$m_w \ddot{x}_w = f_w - k_w x_w \tag{3.10}$$

Taking the Laplace transform of 3.10 and solving for X_w,

$$X_w = \frac{F_w}{m_w s^2 + k_w} \tag{3.11}$$

The force, F_{HM}, applied at the wheel mount is thus:

$$F_{HM} = k_w X_w = \frac{k_w F_w}{m_w s^2 + k_w} \tag{3.12}$$

The decoupled spacecraft's equation of motion is:

$$(m_s + m_w)\ddot{x}_s = f_s - k_s x_s \tag{3.13}$$

so that taking the Laplace transform and solving for X_s yields:

$$X_s = \frac{F_s}{(m_s + m_w)s^2 + k_s} \tag{3.14}$$

In traditional decoupled disturbance analyses, the measured hard-mounted forces are applied directly to the spacecraft model in order to predict its performance metrics. Thus in this case, the force, F_s, applied to the spacecraft must be equated to the hard-mounted force, F_{HM}. Substituting Equation 3.12 for $F_{HM} = F_s$ into 3.14 and simplifying leads to the decoupled input-output relationship between the disturbing force, F_w, and the spacecraft performance metric, X_s:

$$X_s = G_{X_s F_w} F_w \tag{3.15}$$

where:

$$G_{X_s F_w} = \frac{k_w}{m_w(m_s + m_w)s^4 + [k_w(m_s + m_w) + k_s m_w]s^2 + k_s k_w} \tag{3.16}$$

Decoupled Input-Output Relation

In comparing the coupled and decoupled input-output relationships, Equations 3.9 and 3.16, respectively, we see there is only one discrepancy between the two, which lies in the denominator of the transfer function $G_{X_s F_w}$. The decoupled transfer function, 3.16, contains an additional $m_w{}^2$ term multiplying s^4, which suggests that the decoupled analysis over-accounts for the wheel mass by including it in both components of the analysis. Notice that for a spacecraft that is much more massive than the wheel, $m_s \gg m_w$, that these relationships approach one another!

The coupled and decoupled transfer function magnitudes are plotted in Figure 3.2(a) with $m_s = m_w = 1$ and $k_s = k_w = 1$, and they prove to be substantially different. In Figure Figure 3.2(b), they are plotted again for a more realistic mass ratio, with $m_s = 2000$ and $m_w = 10$. As expected, the transfer functions approach one another as the spacecraft and wheel masses approach a realistic ratio.

These results indicate that the traditional *decoupled* disturbance analysis method does not always provide a reliable representation of a coupled system's behavior. In this two-DOF sample problem, we found that for a realistic spacecraft-to-RWA mass ratio, with the spacecraft mass significantly larger than the reaction wheel assembly mass, the decoupled approximation tends toward the coupled solution.

However, one must be cautious in extending this conclusion to more complex, multi-DOF systems. For example, while the ratio of force exerted on a one-DOF body to the acceleration of that body is a constant mass value, the analogous ratio for a flexible, multi-DOF body, with a force applied in one location and acceleration measured in another, is a frequency-dependent value known as the *dynamic mass* or *apparent mass* of the body. So while the two-DOF sample problem suggests that the accuracy of a *decoupled* disturbance analysis depends on the mass ratio of the two bodies, the same conclusion can not necessarily be drawn for multi-DOF systems. This study thus motivates a more detailed investigation into coupled methods of disturbance analysis for multi-DOF systems.

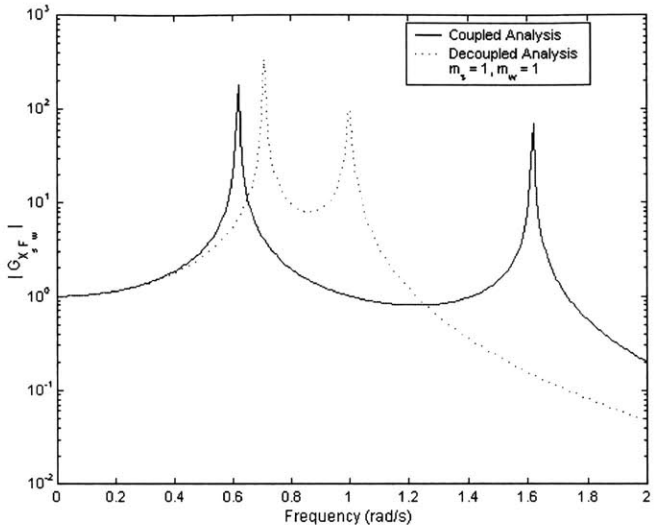

(a) $m_s = 1, m_w = 1$

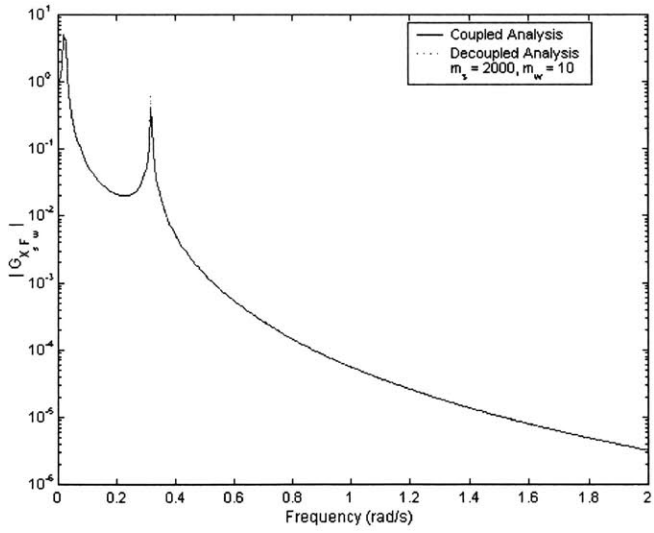

(b) $m_s = 2000, m_w = 10$

Figure 3.2 Two Degree-of-Freedom Sample Problem: Coupled and Decoupled Transfer Functions

3.2 Structural Equations of Motion

We have demonstrated that the traditional method of testing reaction wheels in isolation, and applying these isolated disturbance spectra to a structural model, is not completely

accurate in that it neglects the coupling between the flexible reaction wheel and the structure on which it is mounted. In this section, we introduce the equations of motion of a multi-DOF system in the frequency domain, so that in Section 3.3 we may apply them to a spacecraft-RWA system in order to investigate the approximation being made in the traditional method of disturbance analysis. We will then introduce a method of correction that accounts for spacecraft-RWA structural coupling.

First consider that the equation of motion for a point mass m is:

$$\sum_i f_i = m\ddot{x} \tag{3.17}$$

where f_i is a three-dimensional vector of external forces acting on the mass and $\ddot{x}$ is the three-dimensional vector of resulting accelerations.

The corresponding equation of motion for a *flexible* body with *finite volume*, discretized into a finite number of degrees of freedom, and subjected to external forces and moments is:

$$M\ddot{x} + C\dot{x} + Kx = \sum_i f_i \tag{3.18}$$

where M is the mass matrix, C is the damping matrix, K is the stiffness matrix, x is a vector of generalized degrees of freedom, including displacements and rotations, and f_i is a vector of generalized loads, including forces and moments.

If we shift to the frequency domain by taking the Laplace transform of Equation 3.18, we find:

$$s^2MX(s) + sCX(s) + KX(s) = \sum_i F_i(s) \tag{3.19}$$

where:

$$s = \sigma + j\omega \tag{3.20}$$

$$\mathcal{L}[x(t)] = X(s) \tag{3.21}$$

$$\mathcal{L}[\dot{x}(t)] = sX(s) - x(0^-) \tag{3.22}$$

$$\mathcal{L}[\ddot{x}(t)] = s^2X(s) - sx(0^-) - \dot{x}(0^-) \tag{3.23}$$

$$\mathcal{L}[f_i(t)] = F_i(s) \tag{3.24}$$

and zero initial conditions are assumed, so that $x(0^-) = 0$ and $\dot{x}(0^-) = 0$.

From Equation 3.23,

$$X(s) = \frac{\mathcal{L}[\ddot{x}(t)]}{s^2} = \frac{\ddot{X}(s)}{s^2} \tag{3.25}$$

and substituting into 3.19:

$$M\ddot{X}(s) + \frac{C\ddot{X}(s)}{s} + \frac{K\ddot{X}(s)}{s^2} = \sum_i F_i(s) \tag{3.26}$$

Equation 3.26 can now be written in the same form as Equation 3.17:

$$\sum_i F_i(s) = G_{F\ddot{X}}(s)\ddot{X}(s) \tag{3.27}$$

where $G_{F\ddot{X}}$, the transfer function matrix relating applied loads F_i to accelerations $\ddot{X}$, is defined as:

$$G_{F\ddot{X}}(s) = M + \frac{C}{s} + \frac{K}{s^2} \tag{3.28}$$

Note that while Equation 3.17 applies to a point mass, and forces and accelerations are functions of time, Equation 3.27 applies to a flexible body, and F_i, $\ddot{X}$, and $G_{F\ddot{X}}$ are all frequency-dependent.

3.3 Application to Reaction Wheel Disturbance Testing

One may now attempt to apply Equation 3.27, the frequency-domain equation of motion for a flexible body, to a reaction wheel in order to assess the problem of spacecraft-RWA structural coupling.

3.3.1 Reaction Wheel Equations of Motion

For a spinning reaction wheel attached to a flexible body such as a spacecraft, the loads acting on the wheel can be broken down into two categories:

- disturbance forces and moments, W, caused by the imperfect wheel's spinning motion, and
- reaction forces and moments, F, which occur at the interface between the reaction wheel and the spacecraft.

Thus the equation of motion 3.27 can be written for a reaction wheel as:

$$F(s) = G_{D1}W(s) + G_{D2}\ddot{X}(s) \tag{3.29}$$

where F is a six-dimensional vector of reaction forces and moments at the spacecraft-RWA interface, W is a six-dimensional vector of disturbance forces and torques induced by the spinning wheel, and $\ddot{X}$ is a six-dimensional vector of linear and angular accelerations at the interface. G_{D1} is the transfer function relating F to W, and G_{D2} relates F to $\ddot{X}$.

3.3.2 Coupled Spacecraft-RWA Equations of Motion

If we now consider the coupled spacecraft-RWA system, we can draw a free-body diagram for each component. Since the bodies are connected, their interface forces and moments, F, must be equal in magnitude but opposite in direction, and their linear and angular accelerations, $\ddot{X}$, must be equal in both magnitude and direction, as depicted in Figure 3.3. Here the spacecraft is considered the plant, and the RWA is considered the disturbance to the plant. Z is a vector of performance metrics for the coupled system that typically includes spacecraft displacements, velocities, or accelerations. When the struc-

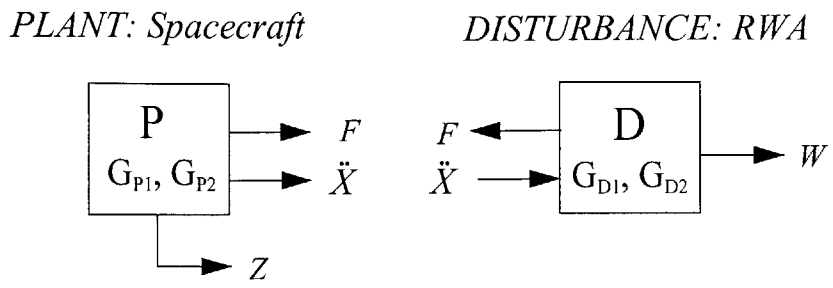

Figure 3.3 Free-Body Diagrams of the Spacecraft and RWA

ture is a space telescope or interferometer, these structural performance metrics may be mapped to optical performance metrics.

Ideally to perform a disturbance analysis for this coupled system, we'd like to find a transfer function that maps disturbances, W, induced by the wheel's spinning, to performance metrics, Z, of the spacecraft. Since this would be the "total" transfer function relating the initial disturbance to the ultimate performance metric, and would include the coupling effect between the RWA and the spacecraft, we will refer to it as G_T.

In Equation 3.29, we defined two transfer functions, G_{D1} and G_{D2}, for the disturbance-inducing RWA, thus relating F, W, and $\ddot{X}$. We now define similar relations for the spacecraft, or the "plant":

$$Z = G_{P1}F \tag{3.30}$$

$$\ddot{X} = G_{P2}F \tag{3.31}$$

so that G_{P1} relates F to the performance metrics Z, and G_{P2} relates F to the interface accelerations $\ddot{X}$.

The relations in Equations 3.29, 3.30, and 3.31 can now be combined to write an expression for G_T. From 3.29 and 3.31:

$$F = G_{D1}W + G_{D2}\ddot{X} = G_{D1}W + G_{D2}G_{P2}F \tag{3.32}$$

Collecting terms and inverting to solve for F,

$$F = [I - G_{D2}G_{P2}]^{-1} G_{D1} W \tag{3.33}$$

We can now relate Z to W using 3.33 and 3.30:

$$\boxed{Z = G_{P1}F = G_{P1}[I - G_{D2}G_{P2}]^{-1} G_{D1} W = G_T W} \tag{3.34}$$

yielding the *coupled* spacecraft-RWA equation of motion. The "total" transfer function is then:

$$\boxed{G_T \equiv G_{P1}[I - G_{D2}G_{P2}]^{-1} G_{D1}} \tag{3.35}$$

If we can find a way to determine each term in Equation 3.35, we will be able to perform a *coupled* disturbance analysis, mapping RWA disturbances, W, to spacecraft performance metrics, Z.

Note that in traditional, *decoupled* spacecraft-RWA disturbance analyses, hard-mounted RWA disturbance tests are performed, in which the wheel is fixed to a rigid surface and spun, and a load transducer between the wheel and the rigid surface is used to measure disturbance loads, F, at the interface. This testing method, which constrains the RWA's acceleration at the interface, corresponds to zeroing $\ddot{X}$ in Equation 3.29 and the right-hand block of Figure 3.3, spinning the wheel to create a disturbance, W, and measuring the resulting reaction loads, F. These measured loads, F, are then applied to the plant using Equation 3.30 to predict the plant performance.

When the wheel is in its *coupled* configuration, however, the interface acceleration is non-zero and depends upon the RWA's own mass and stiffness properties, as well as those of the spacecraft. This is the effect of structural coupling that is neglected in hard-mounted

testing, but is accounted for in Equation 3.34. Thus the error in the traditional *decoupled* method of disturbance analysis lies in the hard-mounted measurement of F, where $\ddot{X}$ is erroneously constrained to zero by the rigid boundary conditions. This fixed boundary condition in vibration tests is often referred to as the "overtest" condition [Scharton, 1995].

3.3.3 Determination of Terms in Coupled Equations of Motion

Equations 3.34 and 3.35 yield spacecraft performances, Z, from RWA disturbances, W, and include spacecraft-RWA structural coupling effects. Hence the determination of all the terms in Equation 3.35 should yield a new, coupled method of spacecraft-RWA disturbance analysis.

The two disturbance terms, G_{D1} and G_{D2}, may be determined experimentally from the reaction wheel to be used on the spacecraft, while the two plant terms, G_{P1} and G_{P2}, may be derived from a model of the spacecraft. In this manner, a *coupled* analysis requires no more than a traditional decoupled analysis: an RWA for experimental testing and a spacecraft *model*; that is, a coupled analysis can be performed without experimental testing of the spacecraft!

Determination of Plant Terms G_{P1} and G_{P2}

We begin by investigating how to determine the spacecraft transfer functions, G_{P1} and G_{P2}. Using a finite element model of the spacecraft, we can obtain these multi-DOF transfer functions by simply specifying an appropriate set of inputs and outputs in each case.

From Equation 3.30, we see that G_{P1} relates a six-axis load vector, F, comprised of three forces, F_x, F_y, and F_z, and three moments, M_x, M_y, and M_z, all applied at the spacecraft-RWA interface node, to a vector of select spacecraft performance metrics, Z. Hence in the structural finite element model, we specify a six-axis load vector applied at the interface node as the input, and a corresponding vector of desired performance metrics, such as the

displacements of certain nodes, as the output. Thus the first dimension of G_{P1} is equal to the number of output performance metrics in the vector Z, and the second dimension is six, equal to the length of the input vector, F.

From Equation 3.31, we see that G_{P2} relates the same six-axis load vector F, applied at the spacecraft-RWA interface node, to a six-axis vector of accelerations, $\ddot{X}$, comprised of three linear accelerations, $\ddot{x}$, $\ddot{y}$, and $\ddot{z}$, and three angular accelerations, $\ddot{\theta}_x$, $\ddot{\theta}_y$, and $\ddot{\theta}_z$, all at the spacecraft-RWA interface node. Hence in the structural finite element model, we again specify a six-axis load vector applied at the interface node as the input, but we now specify a corresponding six-axis acceleration vector at the interface node as the output. Thus the first dimension of G_{P2} is six, equal to the length of the output vector, $\ddot{X}$, and the second dimension is also six, equal to the length of the input vector, F.

Note that many finite element programs will only yield nodal displacements, and not accelerations, as outputs. In this case, one may use the following relation to convert between a transfer function, G_{XF}, yielding displacements to one, $G_{\ddot{X}F}$, yielding accelerations:

$$\boxed{G_{\ddot{X}F}(s) = s^2 G_{XF}(s)} \tag{3.36}$$

This relation is simple to derive. From the definitions of G_{XF} and $G_{\ddot{X}F}$:

$$X(s) = G_{XF}(s)F(s) \tag{3.37}$$

$$\ddot{X}(s) = G_{\ddot{X}F}(s)F(s) \tag{3.38}$$

we can substitute Equation 3.9 for X into 3.37 to find:

$$\frac{\ddot{X}(s)}{s^2} = G_{XF}(s)F(s) \tag{3.39}$$

Multiplying through by s^2 and substituting Equation 3.38 for $\ddot{X}(s)$ yields:

$$\ddot{X}(s) = s^2 G_{XF}(s)F(s) = G_{\ddot{X}F}(s)F(s) \tag{3.40}$$

which is equivalent to Equation 3.36.

Also, note that if a displacement response is given by Equation 3.37, the power spectral density of that response, defined in Section 2.2.2, is:

$$\begin{aligned}
\phi_X(s) &= \lim_{T\to\infty} \frac{1}{2\pi T} E[X(s)X^H(s)] \\
&= \lim_{T\to\infty} \frac{1}{2\pi T} E[G_{XF}(s)F(s)F^H(s)G_{XF}^H(s)] \\
&= G_{XF}(s) \lim_{T\to\infty} \frac{1}{2\pi T} E[F(s)F^H(s)]\ G_{XF}^H(s) \\
&= G_{XF}(s)\phi_F(s)G_{XF}^H(s)
\end{aligned} \tag{3.41}$$

Hence from Equations 3.36 and 3.41, we can write a similar equation relating an output displacement PSD to an output acceleration PSD:

$$\phi_X(s) = G_{XF}(s)\phi_F(s)G_{XF}^H(s) = \frac{G_{\ddot{X}F}(s)\phi_F(s)G_{\ddot{X}F}^H(s)}{s^4} = \frac{\phi_{\ddot{X}}(s)}{s^4} \tag{3.42}$$

or simply:

$$\boxed{\phi_{\ddot{X}}(s) = s^4\phi_X(s)} \tag{3.43}$$

Determination of RWA Term G_{D1}

We now investigate how to experimentally determine the RWA transfer function G_{D1}, and in the next section, G_{D2}. From Equation 3.29, it seems one could determine G_{D1} by performing a hard-mounted RWA test, in which $\ddot{X}$ is constrained to zero, the wheel is spun to create disturbance W, and interface reaction forces $F|_W$ are measured. Here, the notation

$F|_W$ indicates that F is measured with only disturbance W present, and interface accelerations $\ddot{X}$ are constrained to zero:

$$F|_W = G_{D1} W \tag{3.44}$$

In this case, G_{D1} could be extracted from knowledge of $F|_W$ and W. The difficulty in this approach, however, is that one generally cannot determine the disturbance, W, acting on the wheel, but can only measure the resulting interface loads, $F|_W$.

In practice, reaction loads in hard-mounted tests are actually measured in the time-domain as $f(t)|_W$ and are then transferred to the frequency domain using the Fourier transform to obtain $F(\omega)|_W$. If instead, we convert the time histories to spectral density matrix form, $\Phi_{FF}|_W$, as described in detail in Section 2.2.1, we obtain the following relation using Equation 3.44 and a derivation similar to 3.41:

$$\Phi_{FF}|_W = G_{D1} \Phi_{WW} G_{D1}^H \tag{3.45}$$

We can thus write the coupled Equations 3.34 and 3.35 in spectral density form as:

$$\begin{aligned} \Phi_{ZZ} &= G_T \Phi_{WW} G_T^H \\ &= G_{P1}[I - G_{D2}G_{P2}]^{-1} G_{D1} \Phi_{WW} G_{D1}^H [I - G_{D2}G_{P2}]^{-H} G_{P1}^H \end{aligned} \tag{3.46}$$

and substitute Equation 3.45 for $G_{D1}\Phi_{WW}G_{D1}^H$, to find:

$$\Phi_{ZZ} = G_{P1}[I - G_{D2}G_{P2}]^{-1} \Phi_{FF}|_W [I - G_{D2}G_{P2}]^{-H} G_{P1}^H \tag{3.47}$$

or:

$$\boxed{\Phi_{ZZ} = \tilde{G}_T \Phi_{FF}|_W \tilde{G}_T^H} \tag{3.48}$$

where:

$$\tilde{G}_T \equiv G_{P1}[I - G_{D2}G_{P2}]^{-1} \tag{3.49}$$

Thus Equations 3.48 and 3.49 are an equivalent form of the coupled Equations 3.34 and 3.35, but they eliminate the terms G_{D1} and W, which are difficult to determine, and instead express the performance of the coupled spacecraft-RWA system only in terms of known values, G_{P1}, G_{P2}, and G_{D2}, and $\Phi_{FF}|_W$, which is measured in the hard-mounted RWA tests. We have left only to determine G_{D2}.

Determination of RWA Term G_{D2}, "Coupling Correction Term"

Recall that by constraining the wheel to a rigid surface, hard-mounted RWA disturbance tests account only for the $G_{D1}W$ term in Equation 3.29 and neglect the effect of $G_{D2}\ddot{X}$. Since these hard-mounted test results are applied directly to a spacecraft model in order to predict performance in traditional disturbance analyses, they yield only a decoupled approximation to the coupled response. Hence our determination of G_{D2} here will serve as a "coupling correction" to the traditional decoupled method.

In order to determine G_{D2} experimentally for a RWA, the vector of disturbance forces and torques, W, induced by the spinning wheel, must first vanish from Equation 3.29; this occurs whenever the wheel is not spinning. Then a relation must be formed between the vector of interface forces and moments, F, and the vector of linear and angular interface accelerations, $\ddot{X}$, while the wheel is not spinning.

Perhaps the most obvious method of measuring G_{D2} would then be to apply a set of known loads to the wheel interface and measure the resulting interface accelerations. Conversely, known accelerations could be applied, and resulting forces could be measured. For example, the wheel interface could be constrained to a platform moving with known accelerations, and a load transducer could be used to measure the resulting interface loads.

In reality, a combination of these two methods proves best for measuring G_{D2}. The method suggested here is to suspend the RWA in a "free-free" configuration, free of both geometric boundary conditions (displacement constraints) and natural boundary conditions (boundary reaction forces). A white noise disturbance is then applied at the RWA interface, and the resulting six-axis set of interface accelerations and the six-axis set of interface loads are measured by accelerometers and a load transducer, respectively. The 1×1 disturbance, 6×1 interface accelerations, and 6×1 interface loads are all recorded by a data acquisition system and are used to determine both the 6×1 transfer function from the applied disturbance to the interface accelerations and the 6×1 transfer function from the applied disturbance to the interface loads.

Now consider that this test is performed six times, each time applying and measuring a white noise disturbance force or moment in a different direction, and each time measuring the resulting interface accelerations and loads to determine the two 6×1 transfer functions of interest. Then for each test, we can write:

$$\ddot{X}_i(s) = G_{\ddot{X}_i}(s) w_i(s) \tag{3.50}$$

and

$$F_i(s) = G_{F_i}(s) w_i(s) \tag{3.51}$$

where $i = 1, 2, \ldots, 6$, corresponding to the six tests performed, w_i is the 1×1 white noise disturbance applied in test i, $\ddot{X}_i$ is the 6×1 frequency-dependent vector of interface accelerations measured in test i, F_i is the 6×1 frequency-dependent vector of interface loads measured in test i:

$$F_i = \begin{bmatrix} F_x \\ F_y \\ F_z \\ M_x \\ M_y \\ M_z \end{bmatrix}_i \quad \text{and} \quad \ddot{X}_i = \begin{bmatrix} \ddot{X} \\ \ddot{Y} \\ \ddot{Z} \\ \ddot{\Theta}_x \\ \ddot{\Theta}_y \\ \ddot{\Theta}_z \end{bmatrix}_i \tag{3.52}$$

and $G_{\ddot{X}_i}$ and G_{F_i} are the 6×1 transfer functions relating the white noise disturbance in test i to the interface accelerations and loads, respectively.

The white noise disturbance, w_i, by definition has a unity value as a function of frequency, but is applied in a different direction for each test, so that $w \equiv w_i$ for $i = 1, 2, \ldots, 6$. This allows us to combine the information from the six tests and write Equations 3.50 and 3.51 as:

$$[\ddot{X}_i] = G_{\ddot{X}} w \tag{3.53}$$

and

$$[F_i] = G_F w \tag{3.54}$$

where:

$$[\ddot{X}_i] = \begin{bmatrix} | & | & | & | & | & | \\ \ddot{X}_1 & \ddot{X}_2 & \ddot{X}_3 & \ddot{X}_4 & \ddot{X}_5 & \ddot{X}_6 \\ | & | & | & | & | & | \end{bmatrix} \tag{3.55}$$

$$G_{\ddot{X}} = \begin{bmatrix} | & | & | & | & | & | \\ G_{\ddot{X}_1} & G_{\ddot{X}_2} & G_{\ddot{X}_3} & G_{\ddot{X}_4} & G_{\ddot{X}_5} & G_{\ddot{X}_6} \\ | & | & | & | & | & | \end{bmatrix} \tag{3.56}$$

$$[F_i] = \begin{bmatrix} | & | & | & | & | & | \\ F_1 & F_2 & F_3 & F_4 & F_5 & F_6 \\ | & | & | & | & | & | \end{bmatrix} \tag{3.57}$$

and

$$G_F = \begin{bmatrix} | & | & | & | & | & | \\ G_{F_1} & G_{F_2} & G_{F_3} & G_{F_4} & G_{F_5} & G_{F_6} \\ | & | & | & | & | & | \end{bmatrix} \tag{3.58}$$

Solving Equation 3.53 for w and substituting into 3.54 yields:

$$[F_i] = G_F w = G_F G_{\ddot{X}}^{-1} [\ddot{X}_i] \tag{3.59}$$

Since our goal is to determine G_{D2}, the 6×6 matrix relating the three linear and three angular interface accelerations to the three forces and three moments at the interface, we find from Equation 3.59:

$$\boxed{G_{D2} = G_F G_{\ddot{X}}^{-1}} \tag{3.60}$$

Hence the 6×6 frequency-dependent G_{D2} matrix can be determined by performing six free-free tests on the RWA as described above, determining the 6×1 transfer functions $G_{\ddot{X}_i}$ and G_{F_i} for each disturbance test ($i = 1, 2, \ldots, 6$), and combining these transfer functions to solve for G_{D2}, using Equations 3.56, 3.58, and 3.60.

Table 3.1 lists the generalized relationships between force and displacement, velocity, and acceleration. From this table, we see that G_{D2} is the dynamic mass, also known as the apparent mass, of the RWA, since it represents the 6×6 "ratio" of forces to accelerations at the RWA interface.

TABLE 3.1 Generalized Relationships Between Force and Displacement, Velocity, and Acceleration.

$\frac{X(\omega)}{F(\omega)}$	Compliance	$\frac{F(\omega)}{X(\omega)}$	Stiffness
$\frac{\dot{X}(\omega)}{F(\omega)}$	Mobility	$\frac{F(\omega)}{\dot{X}(\omega)}$	Mechanical Impedance
$\frac{\ddot{X}(\omega)}{F(\omega)}$	Accelerance	$\frac{F(\omega)}{\ddot{X}(\omega)}$	Dynamic (Apparent) Mass

The method proposed here for determining the dynamic mass, G_{D2}, was validated using a representative RWA in the Space Systems Laboratory at the Massachusetts Institute of Technology. The experiment will be described in Chapter 4, and the results will be presented and incorporated into a coupled disturbance analysis in Chapter 5.

3.4 Summary

In Section 3.1, a sample problem was presented to motivate a coupled disturbance analysis method for flexible spacecraft-RWA systems. This spring-mass problem demonstrates that the traditional decoupled disturbance analysis method, when applied to a two-DOF coupled system, is only an approximation of a coupled disturbance analysis, but that this approximation is quite accurate if the spacecraft mass is significantly larger than the RWA mass. The limitation here is that the study was performed on a simple, two-DOF system, and the results can not necessarily be extended to complex, multi-DOF systems.

Similarly, the traditional method of spacecraft-RWA disturbance analysis, which applies hard-mounted RWA disturbance spectra to a spacecraft model (that includes the mass of the RWA) in order to predict its performance, is a decoupled approximation of a coupled system. The objective is to investigate the accuracy of this approximation by comparing it to a fully coupled analysis method and to coupled experimental results.

In this chapter, the theory for a coupled disturbance analysis technique has been presented. The suggested method requires both an RWA for experimental testing and a finite element model of the spacecraft, as in the traditional method; however, it improves upon the traditional method by including the RWA's dynamic mass, G_{D2}, as a coupling correction term in the spacecraft's "total" transfer function, $\tilde{G}_T$, which relates the hard-mounted RWA test results, $\Phi_{FF}|_W$, to the spacecraft performance metrics, Φ_{ZZ}.

In summary, a coupled disturbance analysis involves the following steps:

- Determine the spacecraft transfer functions G_{P1} and G_{P2} from the spacecraft finite element model.
- Determine the RWA dynamic mass transfer function, G_{D2}, from free-free testing of the RWA and Equations 3.56, 3.58, and 3.60.
- Determine the RWA disturbance spectra $\Phi_{FF}|_W$ from hard-mounted testing of the RWA.
- Calculate the coupled spacecraft-RWA performance Φ_{ZZ} by substituting G_{P1}, G_{P2}, G_{D2}, and $\Phi_{FF}|_W$ into Equations 3.48 and 3.49.

The laboratory experiments performed to validate this method are described in Chapter 4, and the results are presented in Chapter 5.

Chapter 4

EXPERIMENTAL SETUP

In Chapter 3, a new method of disturbance analysis for structurally coupled systems was introduced. Equations 3.48 and 3.49 were presented for analysis of a flexible structure coupled to a disturbance-inducing reaction wheel assembly (RWA). In order to validate this method, and to determine all the necessary terms as described in Section 3.3.3, three types of laboratory experiments must be performed on the RWA and flexible structure:

1. First the RWA is hard-mounted to an optical bench and spun, and a six-axis load transducer is used to measure the disturbance forces and moments at the rigid bench-RWA interface. This is the traditional method of RWA disturbance testing that yields the disturbance spectra $\Phi_{FF}|_{W}$.
2. The RWA is then suspended in a free-free configuration, white noise disturbances are applied to its interface location, and the resulting six-axis interface accelerations and six-axis interface loads are measured. This is a new testing method introduced in Section 3.3.3 of this thesis; the goal is to provide a coupling correction term, G_{D2}, to the traditional hard-mounted test results obtained in test 1.
3. Finally, the wheel is mounted to a test structure and spun in order to disturb the structure, and measurements of the structure's performance are made. This test is used to validate and compare the decoupled and coupled analysis results.

These three experiments were performed using a representative reaction wheel assembly and a flexible test structure in the Space Systems Laboratory at the Massachusetts Institute of Technology. This chapter describes the three test configurations in detail.

In the next chapter, the results of these tests will be provided. The hard-mounted disturbance spectra obtained in test 1 will first be applied to a finite element model (FEM) of the test structure in order to predict its performance. Next, the structural coupling correction term obtained in test 2 will be appended to the results of test 1, and a coupled analysis will be done to obtain the same performance metrics. Finally, these two analyses will be compared with the performance results from test 3, where the RWA and test structure are physically coupled to one another.

The aim is to show that the addition of the correction term to the RWA disturbance model, when applied to the structural FEM, yields a predicted response of the structure that more accurately represents the true coupled response than the current method of applying only the hard-mounted disturbance spectra. Thus test 3, which requires the actual structure for testing, is used only to validate the coupling correction method.

4.1 Reaction Wheel Hard-Mounted Disturbance Tests

The first test performed on the RWA is the traditional hard-mounted test, where the wheel is attached to a rigid surface and spun at a series of discrete speeds. At each speed, the resulting interface forces and moments are measured to yield disturbance spectra $\Phi_{FF}\big|_{W}$.

4.1.1 Hardware Description

Figure 4.1 shows the representative RWA used in this study in its hard-mounted configuration. The assembly is composed of an aluminum flywheel, a brushless DC motor with a built-in digital tachometer, and two attachment plates. In flight, the RWA would generally be attached to a spacecraft at its bottom surface, so the bottom surface is referred to as the "interface" of the RWA, and the attachment plates are the "interface plates." Some mass and geometric properties of the assembly are listed in Table 4.1.

The RWA interface plates are attached to a load transducer, which is in turn connected by stiff aluminum plates to an optical bench, as shown in Figure 4.1. The load transducer is a

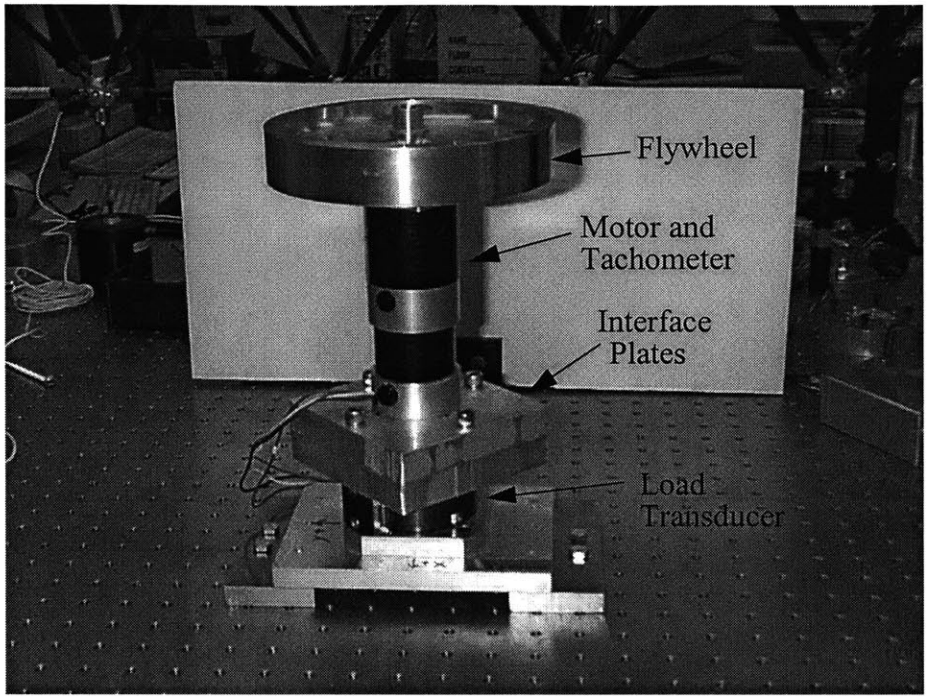

Figure 4.1 Representative Reaction Wheel Assembly in its Hard-Mounted Testing Configuration in the MIT Space Systems Laboratory.

TABLE 4.1 Geometric and Mass Properties of RWA and Supports

Parts	Geometric Properties (cm)	Mass (kg)
Flywheel	Diameter: 17.15 Rim Thickness: 2.54 Inner Thickness: 0.64	2.93 Including Flywheel, Motor, Tachometer, and Top Interface Plate
Motor and Tachometer	Diameter: 5.72 Height: 19.84	
Interface Plates	Thickness: 1.91 Side Length: 11.59	
Load Transducer	Diameter: 7.62 Height: 3.02	2.70, Including Load Transducer, Bottom Interface Plate, Small Aluminum Piece, Screws, Nuts, and Bolts
Aluminum Plates	Total Thickness: 3.81	0.70 for Remaining Aluminum Pieces

six-axis JR3 Universal Force-Moment Sensor System, which measures forces in three axes, f_x, f_y, and f_z, and moments in three axes, m_x, m_y, and m_z. Mass and geometric properties of the load transducer and aluminum plates are listed in Table 4.1. This configuration provides a hard-mounted wheel, with the ability to measure its interface forces and moments.

Figure 4.2 demonstrates how the wheel is spun. First a dual signal generator and data

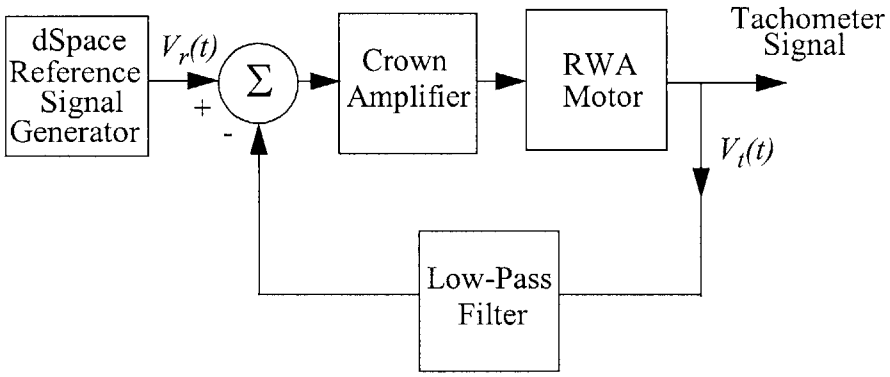

Figure 4.2 Feedback Controller Used to Track the Flywheel's Spin Rate to a Reference Speed.

acquisition unit, called dSpace, is used to produce a reference voltage, $V_r(t)$, corresponding to the desired spin rate. This reference signal is fed into a circuit board controller, along with the tachometer output voltage, $V_t(t)$. The tachometer voltage is passed through a low-pass filter to attenuate high-frequency noise, and then the two signals are compared. The controller output is then the difference between the reference and tachometer voltages, and this output is fed through a Crown DC-200 Series II amplifier to the RWA motor. Note that the flywheel could simply be spun without the controller, by passing the reference voltage, $V_r(t)$, directly through the amplifier to the motor, but this method of rate feedback proves much better in tracking the wheel's spin rate to the reference voltage. The wheel is spun in this manner for a set of speeds ranging from zero rotations per minute (RPM) to 2590 RPM, in increments of ~54 RPM.

4.1.2 Data Collection and Processing

Once the flywheel is rotating at the desired spin rate, the dSpace data acquisition system (DAQ) is used to record the desired data. Figure 4.3 demonstrates the data collection process. The six-axis load transducer unit outputs six channels of data, in the form of voltage

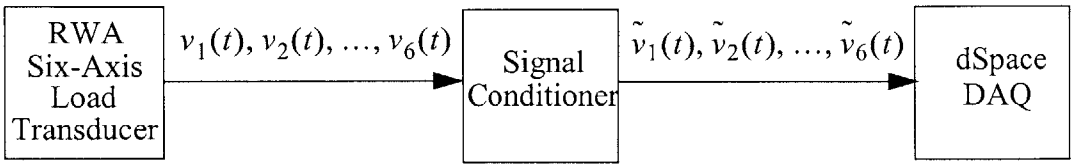

Figure 4.3 Hard-Mounted Disturbance Testing Data Collection Process

time histories. These signals are passed through a signal conditioning unit and into the dSpace data acquisition unit, where they are recorded at a sampling frequency equal to at least twice the bandwidth of interest in order to avoid aliasing, as described in Section 2.2.1. For example, to provide reliable data within a 250 Hz bandwidth, a sampling frequency $f_s = 500$ Hz is used.

Once the six-channel time histories are recorded by the dSpace unit, they must be processed to obtain useful information in the frequency domain. First, the voltage time histories for channels one, two, and three are converted to pounds, and those for channels four, five, and six are converted to inch-pounds using a 6×6 calibration matrix, T, provided by the load transducer manufacturer:

$$\underset{(6\times 1)}{\begin{bmatrix} f_x(t) \\ f_y(t) \\ f_z(t) \\ m_x(t) \\ m_y(t) \\ m_z(t) \end{bmatrix}} = \underset{(6\times 6)}{[T]} \underset{(6\times 1)}{\begin{bmatrix} \tilde{v}_1(t) \\ \tilde{v}_2(t) \\ \tilde{v}_3(t) \\ \tilde{v}_4(t) \\ \tilde{v}_5(t) \\ \tilde{v}_6(t) \end{bmatrix}} \tag{4.1}$$

Note that the calibration matrix, T, is fully populated due to the cross-axis coupling of the load transducer channels. Hence implementation of Equation 4.1 not only converts the six output channels to physical units, but it also decouples them from one another.

The six load histories, $f_x(t)$, $f_y(t)$, $f_z(t)$, $m_x(t)$, $m_y(t)$, and $m_z(t)$, are then converted from English to metric units: the three forces to Newtons, [N], and the three moments to Newton-meters, [N-m].

Finally, the load histories are processed to yield frequency domain information, as described in Section 2.2.1, both in the form of Fourier transforms, $F_x(\omega)$, $F_y(\omega)$, $F_z(\omega)$, $M_x(\omega)$, $M_y(\omega)$, and $M_z(\omega)$, with units [N] and [N-m], and spectral densities with units [N^2/Hz] and [N^2m^2/Hz]. Table 4.2 summarizes the forms of time and frequency domain data obtained from these hard-mounted disturbance tests. As explained in Chapter 3, the

TABLE 4.2 Useful Time and Frequency Domain Forms of RWA Disturbance Data

Data Variables	Description	Domain
$f_x(t), f_y(t), \ldots, m_z(t)$	3 Force and 3 Moment Time Histories	Time
$F_x(\omega), F_y(\omega), \ldots, M_z(\omega)$	3 Force and 3 Moment Fourier Transforms	Frequency
$\Phi_{FF}\|_W(\omega)$	6 × 6 Matrix of Force and Moment Spectral Densities	Frequency

notation, $|_W$, used with the spectral density matrix, $\Phi_{FF}|_W$, indicates that the disturbances were recorded with the wheel hard-mounted and were due only to the wheel's spinning. This spectral density matrix, $\Phi_{FF}|_W$, collected for each wheel speed, is the final product of RWA hard-mounted testing that will be used in the disturbance analysis presented in Chapter 5.

4.2 Reaction Wheel Free-Free Dynamic Mass Tests

The second test performed on the RWA is a "free-free" test, in which the RWA is suspended, free of both geometric (displacement) and natural (force) boundary conditions. This is a new type of test proposed in Chapter 3 of this thesis to supplement the traditional hard-mounted tests in order to account for dynamic coupling between the RWA and its mounting structure.

As described in Section 3.3.1, the goal of this test is to determine the 6×6 dynamic mass transfer function matrix, G_{D2}, relating the three forces and three moments at the RWA interface to the three linear and three angular accelerations at the interface, with no other forces applied and the wheel not spinning. Recall from Chapter 3:

$$F(s) = G_{D1}W(s) + G_{D2}\ddot{X}(s) \tag{3.29}$$

where *W(s)* is the disturbance on the wheel due to its spinning motion; *F(s)* is the vector of three forces, F_x, F_y, and F_z, and three moments, M_x, M_y, and M_z, at the RWA interface; and $\ddot{X}(s)$ is the vector of three linear and three angular accelerations at the RWA interface. Since the wheel is not spinning in these free-free tests, G_{D2} relates *F(s)* to $\ddot{X}(s)$ with $W(s) = 0$. The testing configuration used to determine G_{D2} will now be presented.

4.2.1 Hardware Description

In order to achieve the best approximation to free-free boundary conditions in a 1-g environment, the wheel assembly is suspended, as shown in Figure 4.4, by a soft spring and a string looped through a hole in the flywheel's axis. The spring is soft enough to ensure

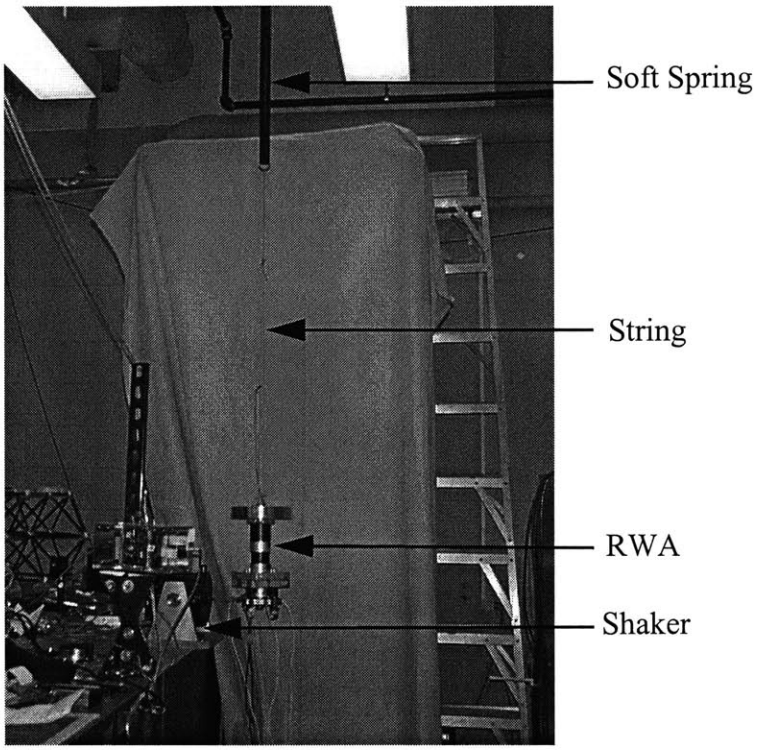

Figure 4.4 Dynamic Mass Testing Free-Free Suspension

that the spring-RWA system's axial and torsional vibration modes are below 1 Hz, and therefore occur at low enough frequency that they will not be detected by the accelerometers used in this experiment. The spring-RWA system's rocking mode is under 3 Hz, which is fortunately still below our frequency range of interest, as will be demonstrated in Chapter 5

A Bruel & Kjaer Type 4800 Electromagnetic Vibration Exciter, also called a shaker, is used to excite the system, and a thin rod, or "stinger," transmits disturbances from the shaker to the RWA, as shown in Figure 4.5. A white noise signal is fed from a Tektronix Fourier Analyzer through a Crown DC-200 Series II amplifier to the shaker, which then disturbs the RWA with an approximately uniform broadband signal.

To measure forces and moments applied at the RWA interface, the same JR3 load transducer used in the hard-mounted tests is used in this case. It is attached to the RWA in the same manner as before, and is shown in Figure 4.5.

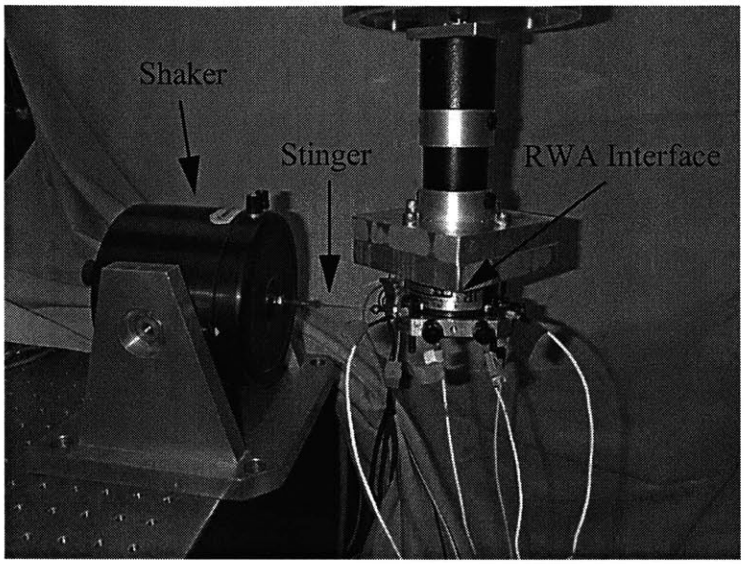

Figure 4.5 Dynamic Mass Testing Excitation Configuration

To measure accelerations at the interface, a set of six Kistler 8630B5 Piezobeam accelerometers is configured at various locations around the interface, as shown in Figure 4.6.

In Section 3.3.3, we discussed that six different loading scenarios are necessary to obtain the desired information from these free-free tests. The six different configurations used in this study are shown in Figure 4.7.

In configuration (a), the stinger is attached to the small plate directly below the load transducer and applies a white noise input in the RWA's $+x$ direction. While this load is primarily an f_x force, it is not applied perfectly along the x axis, and it is not applied exactly at the RWA interface, the load transducer's top surface. Therefore it includes elements of force in three axes and moment in three axes. The load transducer is used to measure the forces and moments at the RWA interface.

Configuration (b) is essentially the same as (a), except that it is rotated by 90 degrees to inject disturbance along the RWA's $+y$ axis. Hence f_y dominates this loading scenario, but finite forces and moments in the other five axes are measured by the load transducer at the RWA interface.

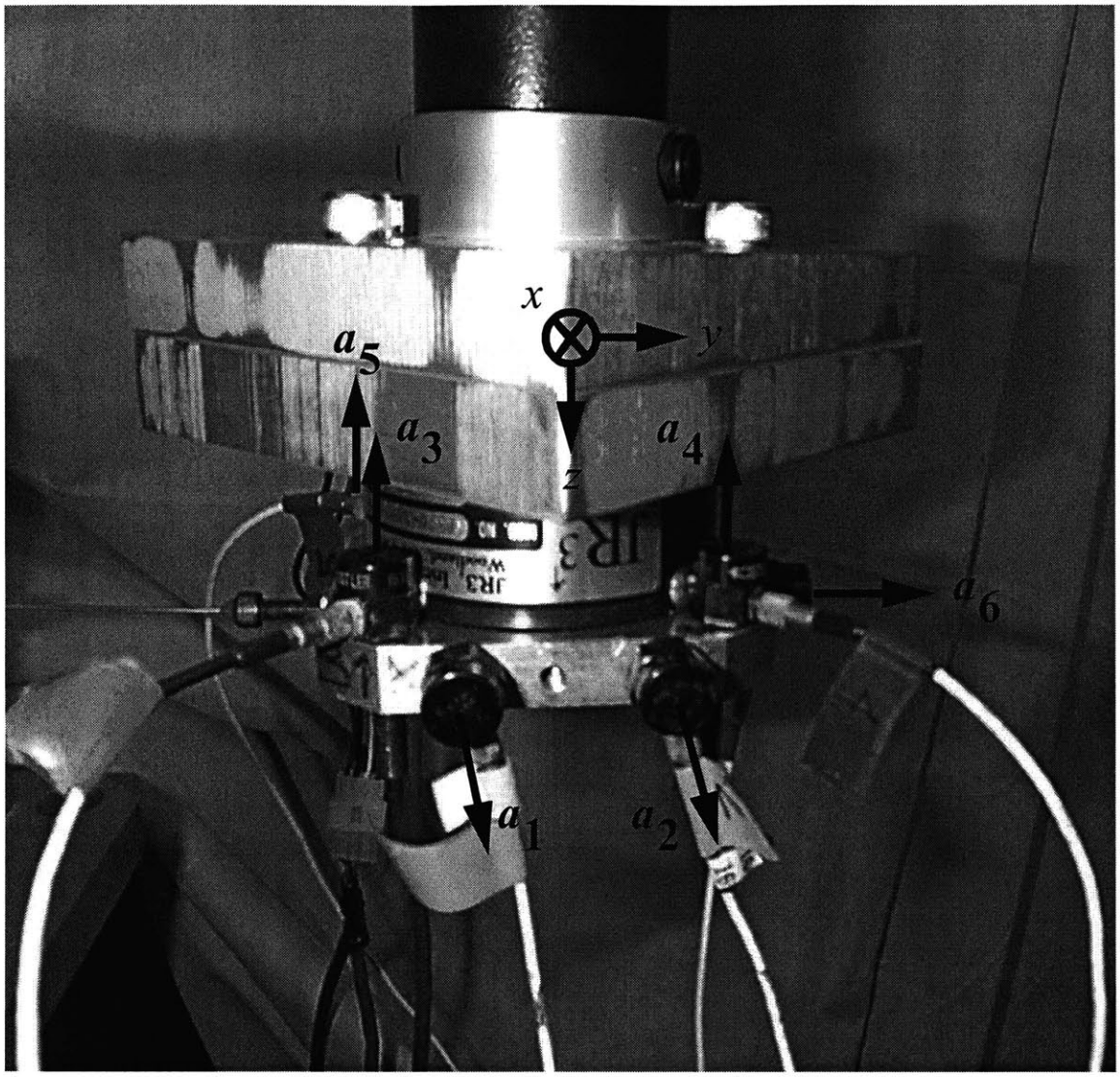

Figure 4.6 Dynamic Mass Testing Accelerometer Configuration

In configurations (c), (d), and (e), a lever arm is used to inject disturbances largely composed of moments at the RWA interface. This lever arm was carefully designed to be stiff enough that its first natural frequency would be beyond the bandwidth of interest, and yet to be light enough that its mass would not significantly alter the dynamic characteristics of the entire assembly. Essentially, this component would be invisible to the test results. While the latter goal was achieved, the former was not, but the assembly was still deemed acceptable. This will be explained further when the results are presented in Section 5.3

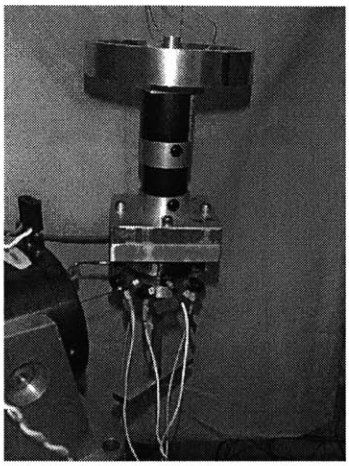

(a) Stinger at Interface: f_x

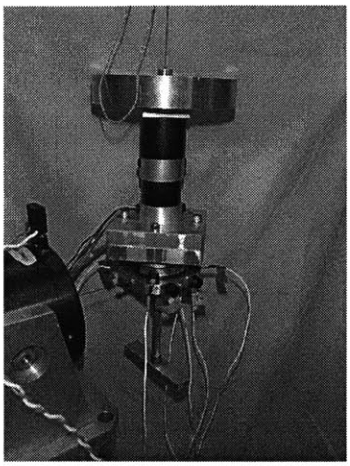

(b) Stinger at Interface: f_y

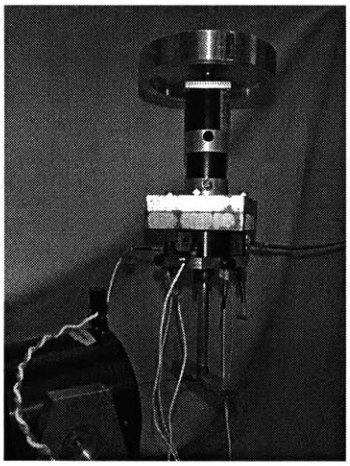

(c) Stinger at Lever Arm Center: f_x, m_y

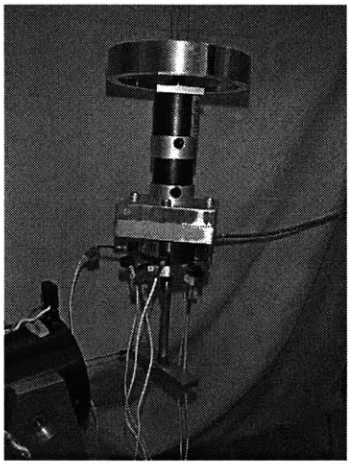

(d) Stinger at Lever Arm End: f_x, m_y, m_z

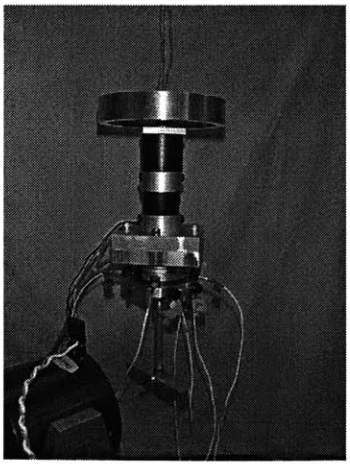

(e) Stinger at Lever Arm Center: f_y, m_x

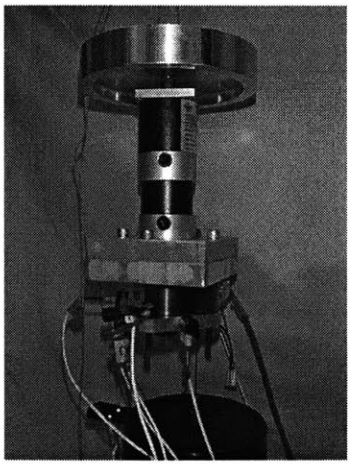

(f) Stinger at Interface: f_z

Figure 4.7 Six Loading Configurations Used for Dynamic Mass Testing of RWA

In configuration (c), a $+x$ force is applied with a moment arm in z, creating a load dominated by f_x and m_y at the interface. In (d), the same force is applied, but with an additional moment arm along y, creating a load composed primarily of f_x, m_y, and m_z. Configuration (e) is essentially the same as (c), but rotated by 90 degrees, so that the primary disturbances lie in f_y and m_x.

Finally, configuration (f) provides a primary disturbance f_z. Hence between the six loading scenarios, all three force and all three moment axes are excited.

4.2.2 Data Collection and Processing

In each of the six loading scenarios shown in Figure 4.7, we are concerned with measuring the white noise disturbance signal being applied to the RWA, the 6×1 vector of linear and angular interface accelerations, and the 6×1 vector of interface forces and moments. Computing $G_{\ddot{X}_i}$ and G_{F_i}, the 6×1 transfer functions from the white noise input to the interface accelerations and loads, respectively, for each of the six tests ($i = 1, 2, \ldots, 6$) will then allow us to determine the RWA's dynamic mass matrix, G_{D2}, as described in detail in Section 3.3.3.

A primary difference between these dynamic mass tests and the RWA disturbance tests described in Section 4.1 is that the dynamic mass tests seek to determine transfer functions, or input-output ratios, of the RWA, while the disturbance tests seek to measure time histories of the RWA disturbances, which are eventually transformed to spectral density functions.

In the disturbance tests, the dSpace DAQ is used to record the disturbance time histories, as described in Section 4.1. However, in these dynamic mass tests, a Tektronix Fourier Analyzer was chosen as a preferable data acquisition system because of its ability to compute transfer functions in real-time. Rather than recording long time histories of the white noise disturbance and the resulting interface accelerations and loads in each test, storing these time histories in large data files, and then calculating the desired transfer functions

from the time histories, we can instead use the Tektronix DAQ to compute several averages of the desired transfer functions in real-time, ensuring high-quality data that can be stored in much smaller data files.

Hence in each of the six tests, the Tektronix DAQ records the white noise signal used to excite the RWA, the six accelerometer voltage outputs, and the six load transducer voltage outputs. It then computes the 6×1 transfer functions $\tilde{G}_{\ddot{X}_i}$ and $\tilde{G}_{F_i}$, which are scaled, "state-transformed" precursors to the desired transfer functions, $G_{\ddot{X}_i}$ and G_{F_i}, for each test.

Recall from the hard-mounted disturbance tests that the six load transducer channels are passed through a signal conditioning unit before being recorded by the data acquisition system; then a 6×6 calibration matrix, T, is used to decouple the signals from one another and to convert from voltages to English units, yielding the three forces and three moments at the RWA interface. Finally, the interface loads are converted to metric units. The same operations must occur in this case to convert $\tilde{G}_{F_i}$, the transfer function computed by the Tektronix analyzer that relates the disturbance voltage to the six conditioned, coupled load transducer voltages, to G_{F_i}, the transfer function relating the disturbance voltage to the actual six-axis interface loads. From Equation 4.1, it can be easily shown that:

$$G_{F_i} = T\tilde{G}_{F_i} \tag{4.2}$$

where G_{F_i} is then scaled to metric units, [N/V] and [N-m/V].

Similarly, $\tilde{G}_{\ddot{X}_i}$ is only a precursor to the desired transfer function, $G_{\ddot{X}_i}$, because the six signals output by the accelerometers are simply six voltages, corresponding to the linear accelerations of the six accelerometers. The six voltages are passed through a Kistler Piezotron Coupler 5128A signal conditioning unit before being recorded by the data acquisition system. The Tektronix analyzer then computes $\tilde{G}_{\ddot{X}_i}$, the transfer function relating the disturbance voltage to the six accelerometer voltages. $\tilde{G}_{\ddot{X}_i}$ is then converted

from units [V/V] to physical units [g/V] using an average accelerometer calibration of 0.984 g/V, specific to the Kistler 8630B5 Piezobeam accelerometers used in this experiment, and is finally converted to metric units, $[(m/s^2)/V]$, for consistency with the load transducer data.

The resulting transfer function, which we call $\tilde{G}^m_{\ddot{X}_i}$, relates the disturbance voltage to the six linear accelerations in metric units. $\tilde{G}^m_{\ddot{X}_i}$ must then undergo a state transformation to yield $G_{\ddot{X}_i}$, which relates the disturbance voltage to the desired six-axis set of linear and angular accelerations at the RWA interface.

From Figure 4.6, one can see that the linear accelerations, $\ddot{x}$, $\ddot{y}$, and $\ddot{z}$, at the interface are determined from:

$$\ddot{x} = -\frac{1}{2}(a_1 + a_2) \tag{4.3}$$

$$\ddot{y} = a_6 \tag{4.4}$$

$$\ddot{z} = -\frac{1}{3}(a_3 + a_4 + a_5) \tag{4.5}$$

and the angular accelerations, $\ddot{\theta}_x$, $\ddot{\theta}_y$, and $\ddot{\theta}_z$, are determined from:

$$\ddot{\theta}_x = \frac{1}{d_{34}}(a_3 - a_4) \tag{4.6}$$

$$\ddot{\theta}_y = \frac{1}{d_{53}}(a_5 - a_3) \tag{4.7}$$

$$\ddot{\theta}_z = \frac{1}{d_{21}}(a_2 - a_1) \tag{4.8}$$

where d_{ij} is the distance between accelerometers i and j:

$$d_{34} = 6.5 \text{ cm}, \quad d_{53} = 6.5 \text{ cm}, \quad d_{21} = 4.0 \text{ cm}$$

This coordinate transformation can be written in a matrix form similar to Equation 4.1:

$$\underset{(6\times 1)}{\begin{bmatrix} \ddot{x}(t) \\ \ddot{y}(t) \\ \ddot{z}(t) \\ \ddot{\theta}_x(t) \\ \ddot{\theta}_y(t) \\ \ddot{\theta}_z(t) \end{bmatrix}} = \underset{(6\times 6)}{\left[T_a\right]} \underset{(6\times 1)}{\begin{bmatrix} a_1(t) \\ a_2(t) \\ a_3(t) \\ a_4(t) \\ a_5(t) \\ a_6(t) \end{bmatrix}} \tag{4.9}$$

where:

$$\left[T_a\right] = \begin{bmatrix} -\frac{1}{2} & -\frac{1}{2} & 0 & 0 & 0 & 0 \\ 0 & 0 & 0 & 0 & 0 & 1 \\ 0 & 0 & -\frac{1}{3} & -\frac{1}{3} & -\frac{1}{3} & 0 \\ 0 & 0 & \frac{1}{d_{34}} & -\frac{1}{d_{34}} & 0 & 0 \\ 0 & 0 & -\frac{1}{d_{53}} & 0 & \frac{1}{d_{53}} & 0 \\ -\frac{1}{d_{21}} & \frac{1}{d_{21}} & 0 & 0 & 0 & 0 \end{bmatrix} \tag{4.10}$$

From Equation 4.9, it is easy to see that $G_{\ddot{X}_i}$ can be obtained by a similar state transformation of $\tilde{G}^m_{\ddot{X}_i}$:

$$G_{\ddot{X}_i} = T_a \tilde{G}^m_{\ddot{X}_i} \tag{4.11}$$

yielding the desired transfer function from the disturbance voltage to the six-axis set of linear and angular accelerations at the RWA interface.

Once G_{F_i} and $G_{\ddot{X}_i}$ have been determined for each of the six test configurations ($i = 1, 2, \ldots, 6$), G_{D2} is calculated as shown in Section 3.3.3. These results will be presented in Chapter 5.

4.3 Structure-Reaction Wheel Coupled Tests

In order to validate the decoupled and coupled disturbance analysis methods, it is necessary to physically couple the RWA with a flexible test structure and determine the coupled performance.

4.3.1 Hardware Description

The structure used in this study, shown in Figure 4.8, is a three-longeron, six-bay cantilever-like truss structure originally designed and built for disturbance and sensitivity analysis studies. It is composed primarily of truss members connected at the nodes by balls

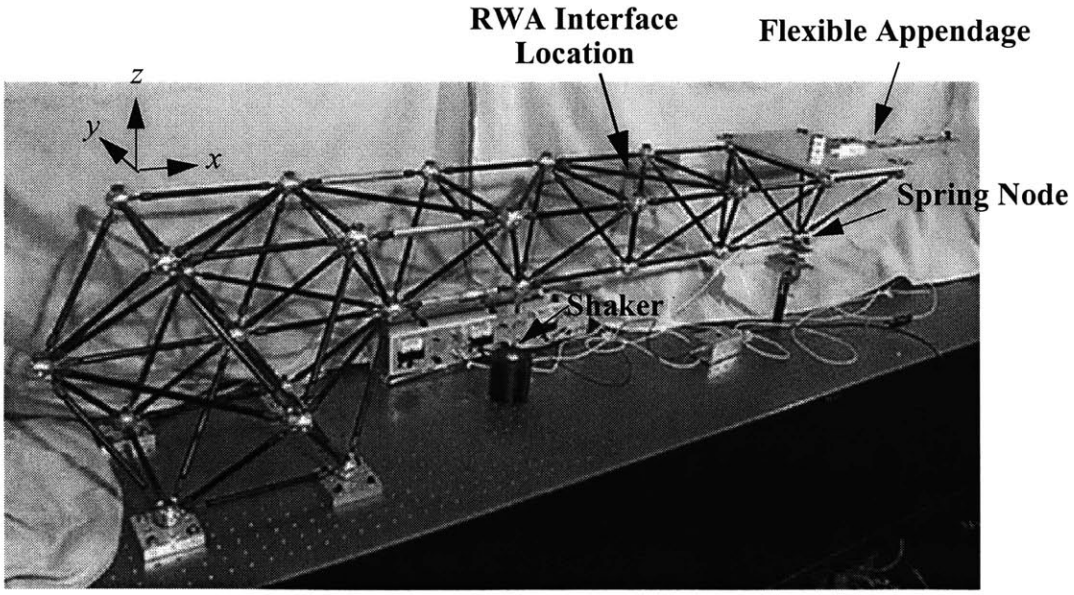

Figure 4.8 Flexible Truss Test Structure used for Validation of Coupled Disturbance Analysis.

with threaded holes, and it is fixed to a rigid optical bench by four nodes at the root. At its tip, supported by a stiff spring, lies an aluminum plate and a flexible appendage. A

detailed description of this test bed, including photographs and a list of parts, can be found in [Gutierrez, 1999].

A few modifications were made to the structure, including the addition of the RWA and its support plate on the third bay from the tip, as shown in Figure 4.9. A finite element model

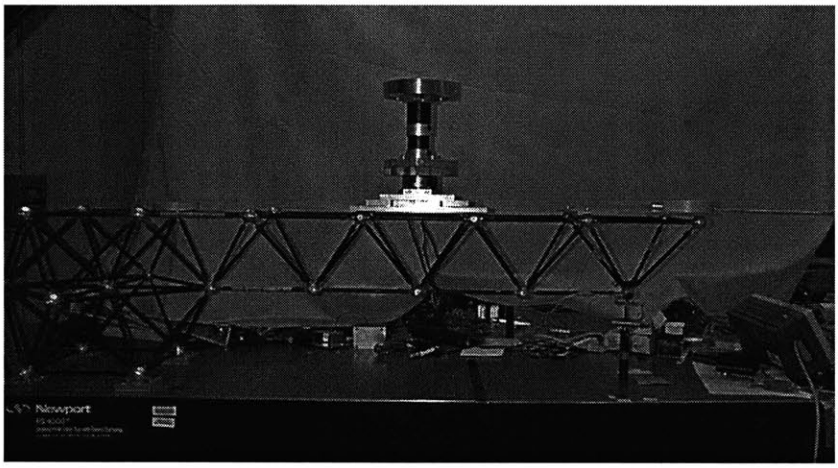

Figure 4.9 RWA in Coupled Configuration with Test Structure.

of the structure was inherited from the previous configuration and was updated to account for these changes. In the model, the RWA was modeled as a lumped mass, with mass estimated from a weight measurement and rotary inertia properties estimated from geometry measurements. The RWA support plate had been modeled in a previous configuration as attached at a different bay location, so this plate was simply shifted in the model to its new location.

Finite Element Model and System Identification

In order to validate the updated finite element model, a system identification laboratory experiment was performed on the structure in its new configuration. The input is a disturbance force in z, applied by a Bruel & Kjaer Type 4810 Mini Shaker at the node shown in Figure 4.8, and the performance metrics are displacements in three locations: one in z at the appendage tip and two at the spring node, in z and y, respectively. (Note that the per-

formances are actually measured by accelerometers in each location, but Equation 3.36 allows us to move between acceleration and displacement transfer functions.)

Figure 4.10 shows the three disturbance-to-performance transfer functions, both as predicted by the updated finite element model and as measured in the system identification test, and Table 4.3 lists the four dominant resonant frequencies, as predicted and measured. From Table 4.3, we see that the model captures the first two resonances quite well, with only a ~0.6 % error, but that it strays from the measured data at higher frequencies.

Much insight can be gained by studying the cumulative RMS values of the transfer functions, plotted above their respective transfer functions in Figure 4.10. (See Section 2.3 for a definition of the cumulative RMS function.) Notice that the cumulative RMS functions gain most of their magnitude from the first two modes, and are hardly effected by the higher modes. This suggests that the accuracy of the first two modes is the primary concern in validating this finite element model, and that the discrepancy in the higher modes is acceptable.

Also note that the test structure's two most influential modes lie at 21.7 Hz and 28.4 Hz, and since the representative RWA used in this study can be spun up to 2590 RPM, or 43 Hz, we will be able to excite these structural modes by spinning the wheel at certain speeds. Also, since the wheel itself is flexible, it will in turn be excited by the resonances of the structure. Hence this structure is quite suitable for a coupled study, since it will encounter dynamic coupling with the RWA.

Coupled Validation Test

In the coupled validation test, the wheel, mounted as shown in Figure 4.9, is spun in order to disturb the structure, and three accelerometers are used to measure the same performance metrics as in the system identification test. These are the "truly" coupled performance metrics which will be used to validate both the decoupled and coupled disturbance analysis methods presented in Chapter 5.

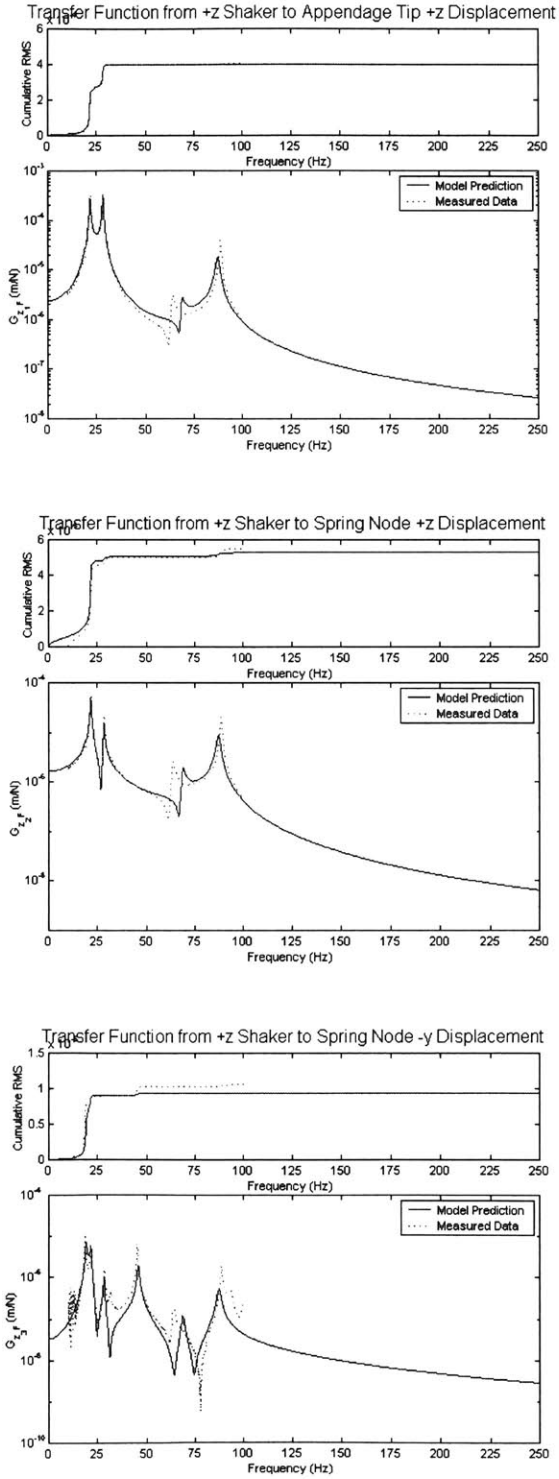

Figure 4.10 Test Structure Transfer Functions: Finite Element Model Prediction vs. Measured Data

TABLE 4.3 Test Structure Resonant Frequencies

Frequency Number	Model Prediction (Hz)	Measured Data (Hz)	Model Error (%)
1	21.6	21.7	-0.6
2	28.3	28.4	-0.5
3	68.9	63.8	+8.0
4	87.1	88.6	-1.7

The wheel is spun just as in the hard-mounted disturbance tests, as diagrammed in Figure 4.2, with the only exception being the change in boundary conditions. It is spun at each of the speeds used in the hard-mounted tests, and at each speed, three of the same Kistler 8630B5 Piezobeam accelerometers used in the free-free dynamic mass tests are used to measure the structure's performance metrics.

4.3.2 Data Collection and Processing

Since the only data recorded in these coupled tests are three accelerometer outputs for each wheel speed, the data collection and processing proves to be fairly simple. The accelerometer signals are passed through the same signal conditioning unit used in the dynamic mass tests and are recorded by the dSpace DAQ as voltage time histories. The same conversion factors used in the dynamic mass tests are then used to convert the accelerations from volts to metric units, [m/s^2]. Finally, the time histories are processed to yield power spectral densities of the accelerations, which are then converted to power spectral densities of displacements using Equation 3.43.

4.4 Summary

In this chapter, three different types of laboratory experiments have been described:

1. the RWA hard-mounted tests, which yield a 6×6 spectral density matrix, $\Phi_{FF}|_W$, for each wheel speed.
2. the RWA free-free dynamic mass tests, which yield the 6×6 coupling correction matrix, G_{D2}, and

3. the coupled validation tests, which yield three performance metrics for each wheel speed.

In Chapter 5, the experimental results will be presented. Test 1 results will be applied to the structural finite element model to predict its performance, as done in a traditional *decoupled* disturbance analysis. Test 2 results will then be appended to those of test 1 and will be reapplied to the model in order to perform a *coupled* disturbance analysis. Finally, test 3 results will be presented and compared to the decoupled and coupled disturbance analyses in order to determine which better predicts the true coupled performance.

Chapter 5

EXPERIMENTAL RESULTS

In Chapter 3, the theory for a new method of disturbance analysis that accounts for the structural dynamic coupling of a flexible structure and a disturbance-inducing reaction wheel assembly (RWA) was presented. This method utilizes free-free dynamic mass tests of the RWA to supplement the hard-mounted disturbance test data typically applied to a structural model in order to predict the coupled system's behavior. The proposed experiments were performed using a representative RWA and a flexible test structure in the Space Systems Laboratory at the Massachusetts Institute of Technology, as described in detail in Chapter 4.

This chapter presents the RWA hard-mounted and free-free test data and combines these results with outputs from the test structure finite element model (FEM) in order to perform two analyses: a traditional decoupled disturbance analysis and the proposed coupled analysis. The coupled experimental results are also presented for validation of the two analysis methods.

5.1 Reaction Wheel Disturbance Test Results

Hard-mounted tests of the reaction wheel, described in Section 4.1, were performed for a set of discrete wheel speeds ranging from zero revolutions per minute (RPM) to 2590 RPM, in increments of ~54 RPM, resulting in a spectral density matrix, $\Phi_{FF}|_{W}$, for each wheel speed. In addition, coupled disturbance tests with the wheel mounted to the test

structure described in Section 4.3.1 were performed to investigate the difference in measured interface forces and moments between the hard-mounted and coupled configurations. The results of both tests are presented here.

5.1.1 Hard-Mounted Disturbance Spectra

These hard-mounted RWA disturbance tests were described in great detail in Section 4.1. The results are presented in Figure 5.1, where the disturbance spectra collected for all the wheel speeds are combined into six three-dimensional plots, one for each axis of disturbance. Plots (a) - (f), respectively, represent the disturbance power spectral densities (PSDs) ϕ_{F_x}, ϕ_{F_y}, ϕ_{M_x}, ϕ_{M_y}, ϕ_{F_z}, and ϕ_{M_z}, which are the diagonal components of the spectral density matrix $\Phi_{FF}|_W$, plotted against frequency (x-axis) for each wheel speed (y-axis). These plots are known as "waterfall plots," since for each *discrete* wheel speed at which disturbances are measured, the frequency information seems to "flow" continuously in a spectrum parallel to the x-axis.

Notice that the F_x and F_y spectra are very similar in magnitude and frequency, due to the near axial symmetry of the RWA. The same is true for the M_x and M_y spectra. Note also that the F_z spectrum has much larger primary-harmonic and peak magnitudes than the F_x and F_y spectra, indicating that axial disturbance forces caused by the spinning RWA are significant compared to radial disturbance forces, and therefore should never be neglected when performing a disturbance analysis on the mounting structure.

Figure 5.1 also demonstrates that ϕ_{M_z} is generally over two orders of magnitude smaller than ϕ_{M_x} or ϕ_{M_y}. This is due to the fact that the flywheel is free to rotate about its z-axis and thus causes very little disturbance moment about z. For this reason, M_z spectra are often neglected in disturbance analyses.

In all of the plots shown in Figure 5.1, the primary harmonic is clearly present. (A discussion of primary and higher harmonics was presented in Section 2.1.) At the fastest spin rate, 2590 RPM, the primary harmonic occurs at an equivalent 43 Hz, as seen in each of

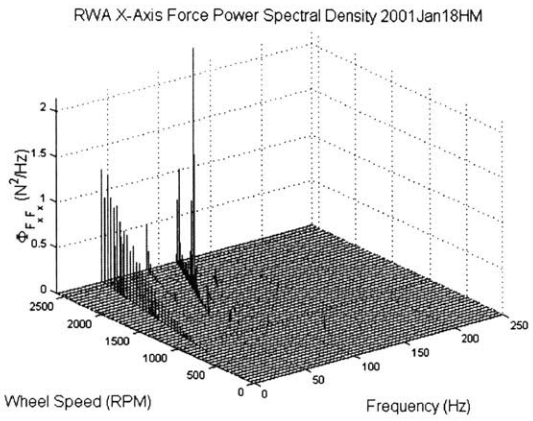

(a) $\Phi_{F_xF_x}$

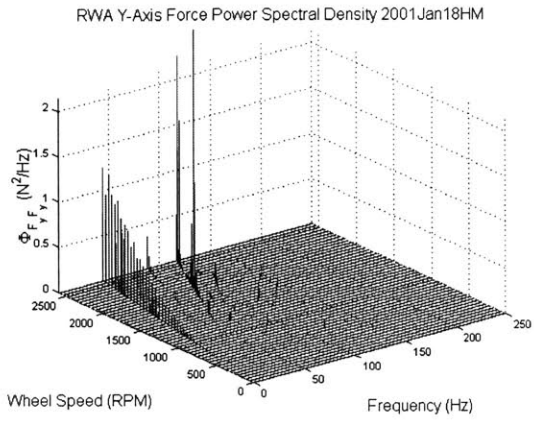

(b) $\Phi_{F_yF_y}$

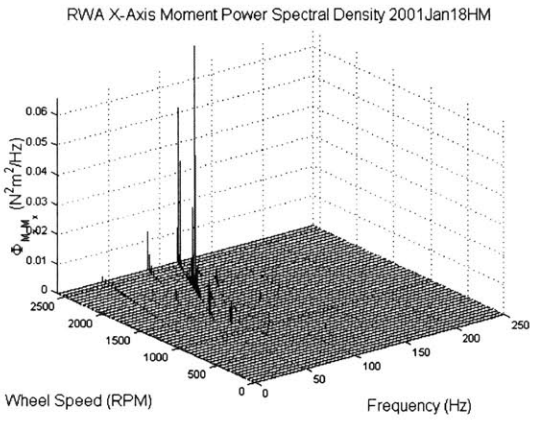

(c) $\Phi_{M_xM_x}$

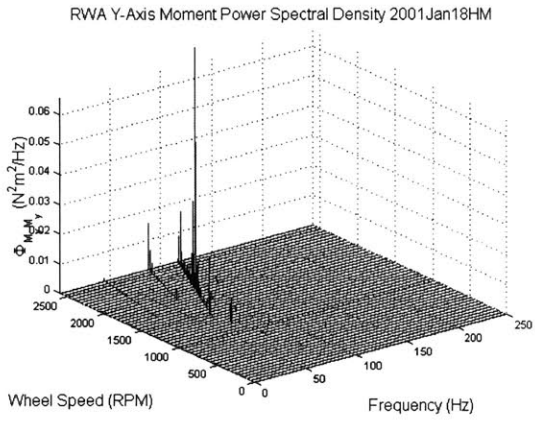

(d) $\Phi_{M_yM_y}$

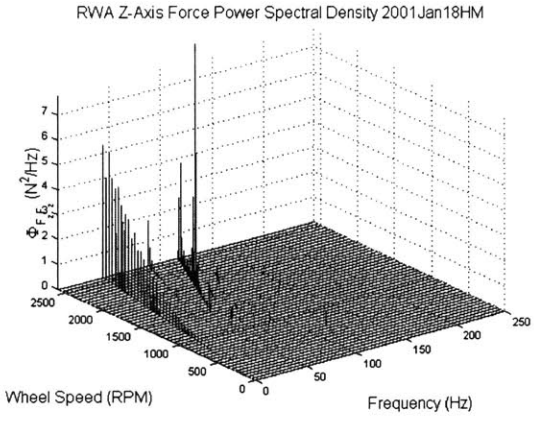

(e) $\Phi_{F_zF_z}$

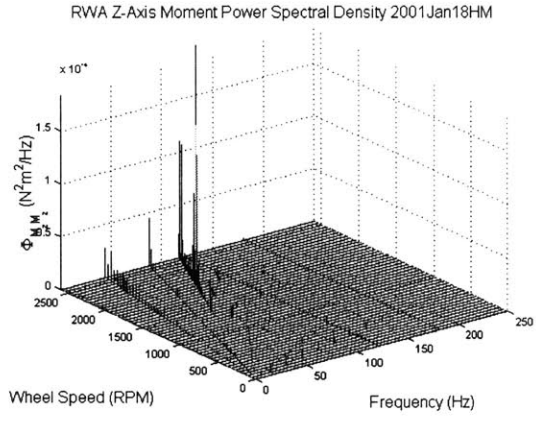

(f) $\Phi_{M_zM_z}$

Figure 5.1 Representative Reaction Wheel Hard-Mounted Disturbance Spectra

the plots. Perhaps the most interesting feature of these hard-mounted spectra, however, is the fact that the peak disturbance magnitudes are not due to the primary harmonic, but rather to amplifications within the higher harmonics. The magnitudes of the higher harmonics are generally smaller than that of the primary, but when a harmonic "crosses" a structural resonance of the RWA, amplifications or "spikes" of this type occur. Clearly the peak magnitudes are caused by the interaction of the wheel flexibility with the higher harmonics of disturbance. In the next section, we will find this is not the case when the wheel is mounted to the structure, and we will discuss the implications of this.

5.1.2 Coupled Disturbance Spectra

While only hard-mounted RWA disturbance tests are necessary to perform either a traditional decoupled disturbance analysis or the proposed coupled analysis, disturbance tests were also performed with the RWA mounted to the test structure described in Section 4.3. The sole purpose of these coupled disturbance tests is to compare the hard-mounted spectra with the actual disturbances induced when the wheel is mounted on the structure. Finding that the hard-mounted and coupled spectra are, in fact, different will further motivate the development of a coupled disturbance analysis approach.

The coupled disturbance spectra are shown in Figure 5.2. Unlike the hard-mounted spectra in Figure 5.1, the peak disturbance magnitudes of the coupled spectra are *not* dominated by amplifications of the higher harmonics, but rather by the primary harmonic and *its* interaction with structural resonances of the wheel and test structure. Also notice that the F_x and F_y spectra in Figures 5.2 (a) and (b), respectively, are no longer similar due to the *asymmetry of the test structure*; the same holds true for the M_x and M_y spectra in Figures 5.2 (c) and (d), respectively.

Perhaps better insight into the differences between the hard-mounted and coupled spectra can be gained by viewing surface plots of the spectra from a -z perspective, looking down upon the data "surfaces." Figure 5.3 shows the six hard-mounted and six coupled spectra from this perspective, where the lighter areas indicate larger disturbance magnitudes.

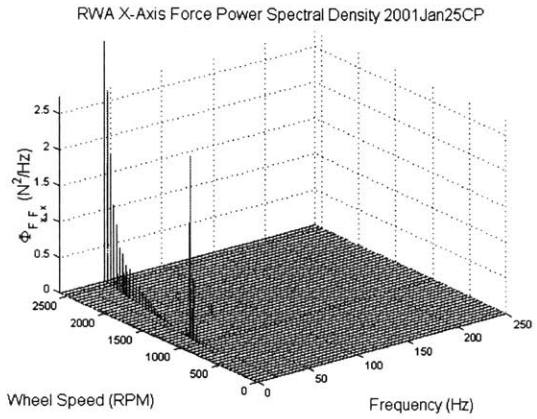

(a) $\Phi_{F_xF_x}$

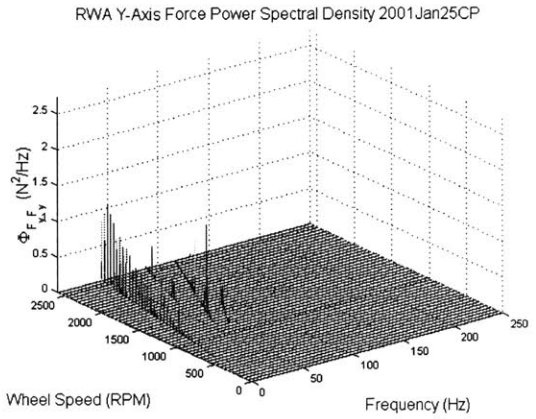

(b) $\Phi_{F_yF_y}$

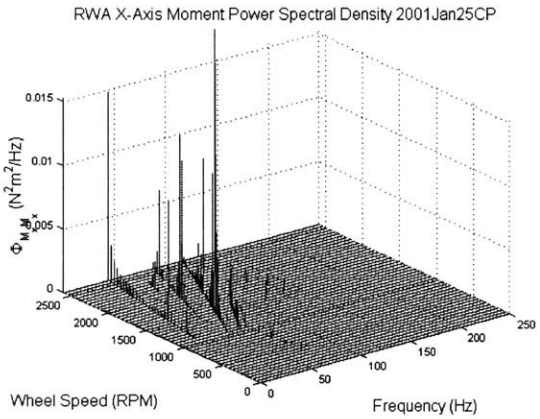

(c) $\Phi_{M_xM_x}$

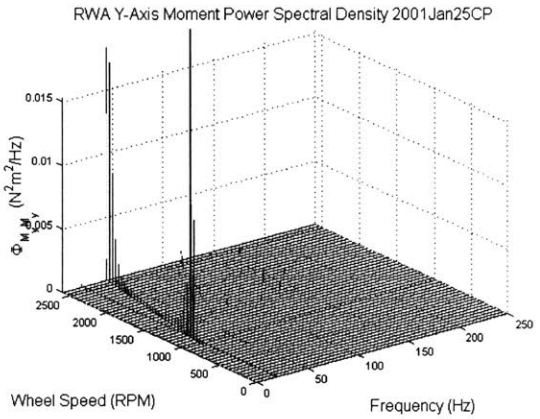

(d) $\Phi_{M_yM_y}$

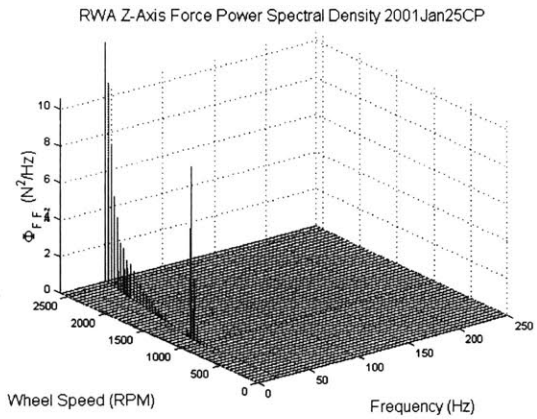

(e) $\Phi_{F_zF_z}$

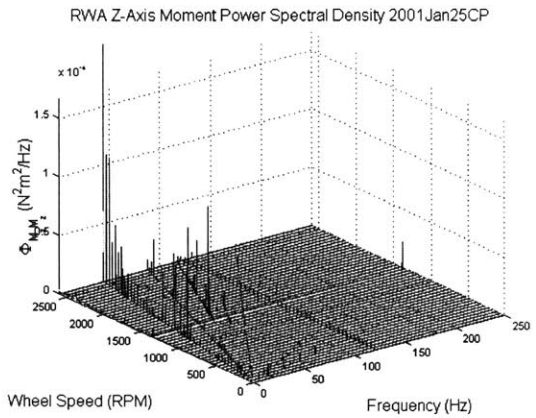

(f) $\Phi_{M_zM_z}$

Figure 5.2 Representative Reaction Wheel Coupled Disturbance Spectra

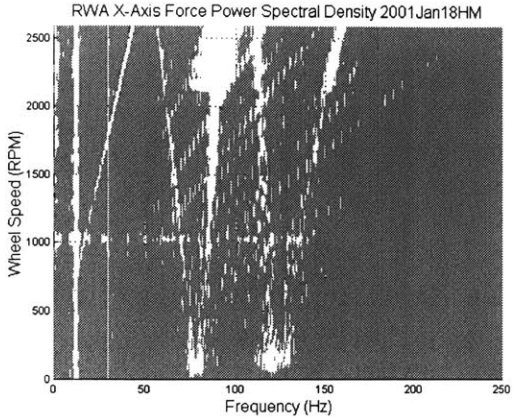

(a) Hard-Mounted $\Phi_{F_xF_x}$

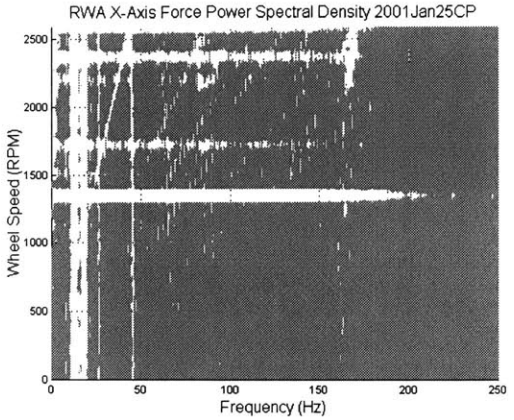

(b) Coupled $\Phi_{F_xF_x}$

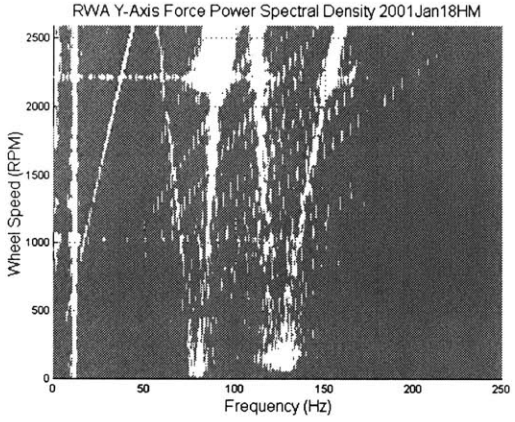

(c) Hard-Mounted $\Phi_{F_yF_y}$

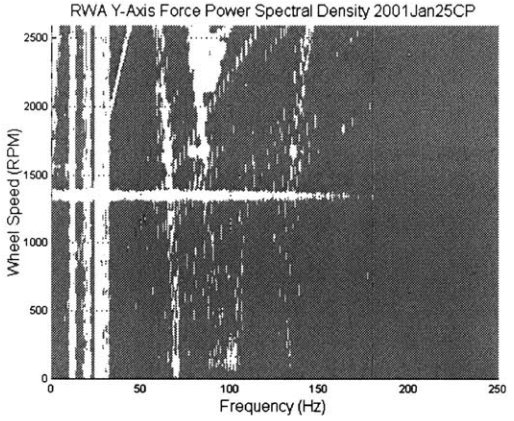

(d) Coupled $\Phi_{F_yF_y}$

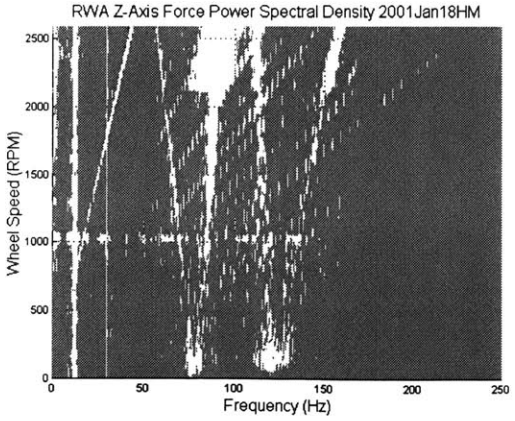

(e) Hard-Mounted $\Phi_{F_zF_z}$

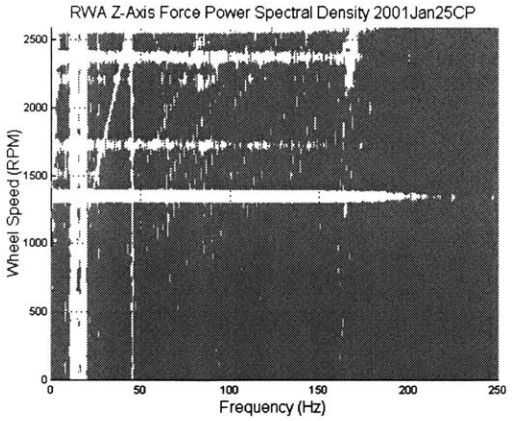

(f) Coupled $\Phi_{F_zF_z}$

Figure 5.3 Hard-Mounted and Coupled Disturbance Spectra: -z Surface View

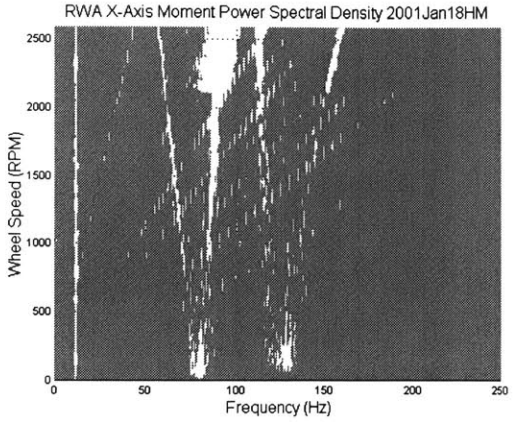

(g) Hard-Mounted $\Phi_{M_xM_x}$

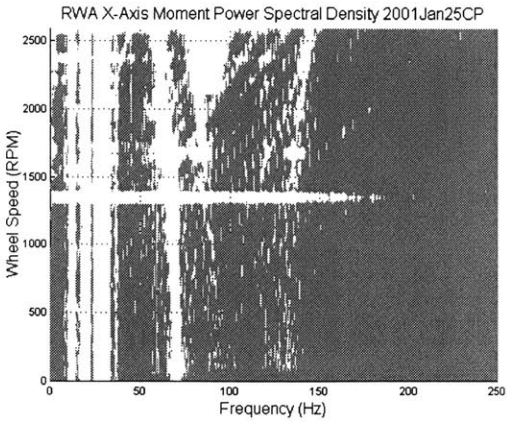

(h) Coupled $\Phi_{M_xM_x}$

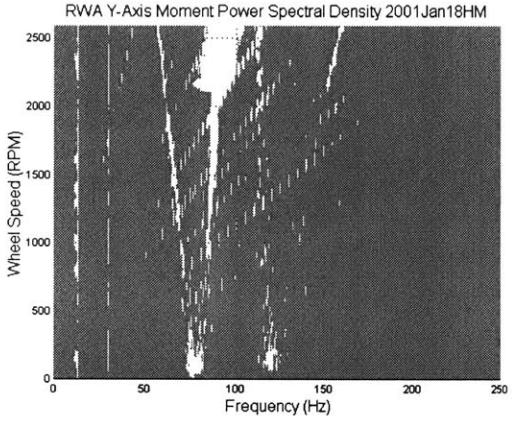

(i) Hard-Mounted $\Phi_{M_yM_y}$

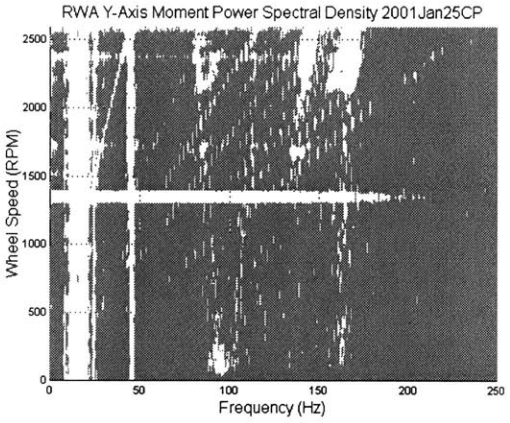

(j) Coupled $\Phi_{M_yM_y}$

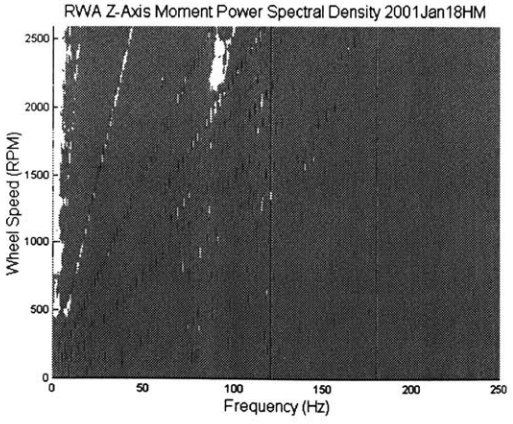

(k) Hard-Mounted $\Phi_{M_zM_z}$

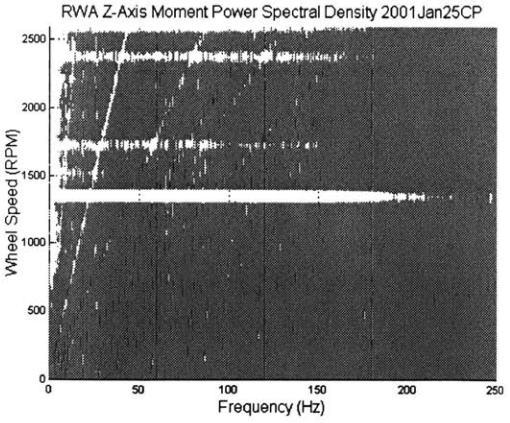

(l) Coupled $\Phi_{M_zM_z}$

Figure 5.3 Hard-Mounted and Coupled Disturbance Spectra: -z Surface View

From this perspective, the primary and several higher harmonics are visible as lines emanating from the origin, and the structural resonances of both the wheel and the test structure can be seen as lines of constant frequency or wheel speed. These plots offer the additional benefit that they allow easy detection of the frequencies and wheel speeds at which structural resonances cross the wheel harmonics.

In Section 4.3.1, we found that the test structure has resonances at 21.7, 28.4, 63.8, and 88.6 Hz, with the 21.7 Hz mode being dominant. These test structure modes are clearly visible as both vertical and horizontal lines at the corresponding frequencies in the coupled test spectra displayed in Figure 5.3. As expected, they do not appear in the hard-mounted spectra.

Conversely, the hard-mounted spectra contain lines that appear only faintly, if at all, in the coupled disturbance spectra. These lines correspond to RWA structural resonances. (The three dominant vibrational modes of a reaction wheel were introduced in Section 2.1.) For example, the line emanating from ~75 Hz, almost constantly for all wheel speeds, has been identified as the axial translation mode of this wheel. Also, the V-shaped pair of lines emanating from ~120 Hz represent the positive and negative whirl components of the rocking mode. (The rocking mode splits into these two distinct natural frequencies at finite wheel speeds due to gyroscopic effects. The negative whirl opposes the rotation, while the positive whirl agrees with it.) There is an additional mode, also emanating from ~75 Hz but decreasing in frequency with increased wheel speed, that has not been positively identified.

Clearly the hard-mounted disturbance spectra that are typically measured in isolation and applied to spacecraft models are different from the actual disturbances induced in the coupled system. A closer look at Figures 5.1, 5.2, and 5.3 demonstrates that the hard-mounted spectra have enormous amplifications where the harmonics cross the *wheel* modes, whereas the coupled spectra have enormous amplifications where the harmonics cross the *mounting structure's* modes.

Further, the hard-mounted spectra appear to have a higher frequency content, or a stronger representation of the higher harmonics, than the coupled spectra. And aside from the resonant amplifications, the hard-mounted harmonic amplitudes are generally larger. This trend of higher harmonic frequencies and larger harmonic amplitudes is due to the infinite mechanical impedance of the hard-mounted test interface, which is fixed to have zero motion. For this reason, hard-mounted vibration testing is often referred to as an "overtest" condition [Scharton, 1995].

5.2 Reaction Wheel Free-Free Dynamic Mass Test Results

Free-free dynamic mass tests of the reaction wheel, described in detail in Section 4.2, were performed with the wheel suspended and not spinning, resulting in a dynamic mass matrix, $G_{D2}(\omega)$, for the RWA. As described in Section 3.3, this 6×6 frequency-dependent matrix relates the six interface loads, F_x, F_y, F_z, M_x, M_y, and M_z, to the six interface accelerations, $\ddot{X}$, $\ddot{Y}$, $\ddot{Z}$, $\ddot{\Theta}_x$, $\ddot{\Theta}_y$, and $\ddot{\Theta}_z$, of the RWA.

Select components of the dynamic mass matrix, G_{D2}, are plotted in Figure 5.4. The small resonance appearing at ~53 Hz in each component is due to the lever arm that was appended to the RWA for testing purposes. The arm was designed to be low in mass and high in fundamental frequency so it would not affect the test data. However, as mentioned in Section 4.2.1, the fundamental frequency was not high enough to be outside the bandwidth of these tests.

In order to determine the effect of this mode on the data, the cumulative RMS functions of the components of G_{D2} were computed, and a select few are plotted above the corresponding magnitudes in Figure 5.4. (See Section 2.3 for a definition of the cumulative RMS function.) From the cumulative RMS plots, we see that the lever arm mode does not visibly contribute to the total RMS; hence we do not expect this mode to corrupt the final results of the coupled analysis.

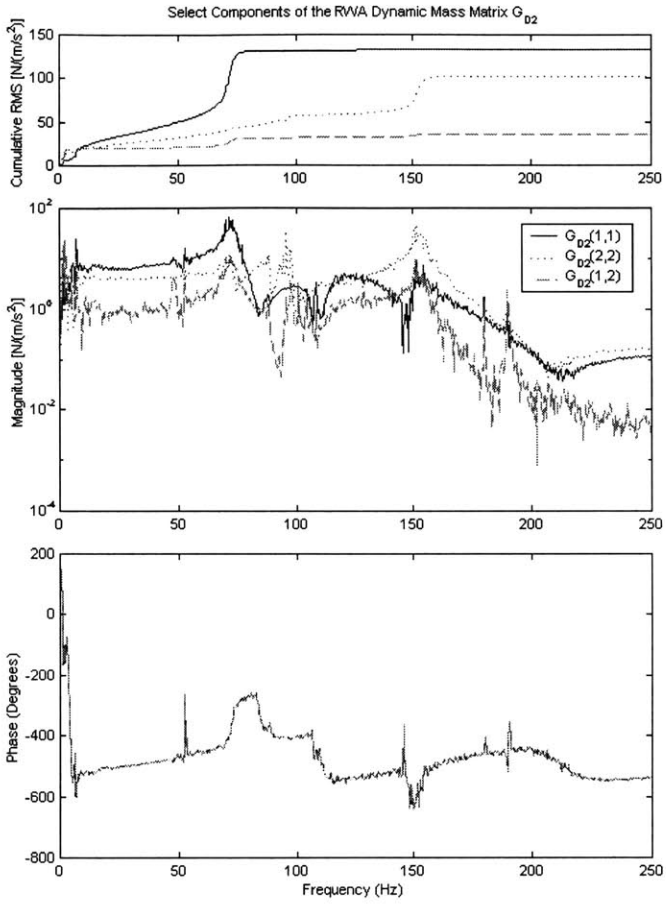

Figure 5.4 Cumulative RMS and Magnitude of Select Components of the Dynamic Mass Matrix, G_{D2}.

The dynamic mass matrix, G_{D2}, will be incorporated into a coupled disturbance analysis in the following section.

5.3 Coupled Analysis Results

As derived in Chapter 3, a coupled analysis of a flexible structure and disturbance-inducing RWA spinning at a discrete speed yields the system performance in spectral density form as:

$$\Phi_{ZZ} = \tilde{G}_T \Phi_{FF}\big|_W \tilde{G}_T^{\,H} \tag{3.48}$$

where $\Phi_{FF}\big|_W$ is the matrix of hard-mounted disturbance spectra measured at a discrete wheel speed, and:

$$\tilde{G}_T \equiv G_{P1}[I - G_{D2}G_{P2}]^{-1} \tag{3.49}$$

is the *coupled* or "total" transfer function relating hard-mounted disturbance spectra to *coupled* system performance spectra. Recall that G_{P1} is the transfer function relating the test structure's interface forces to its performance metrics, and G_{P2} relates its interface forces to its interface accelerations. Hence G_{P2} is the dynamic mass matrix of the test structure, with all inputs and outputs defined at the structure-RWA interface location. Finally, G_{D2} is the dynamic mass matrix of the RWA, measured in free-free laboratory tests described in Section 4.2.

In comparison, a traditional decoupled analysis is performed by using only the plant transfer function, G_{P1}, in place of the coupled transfer function, $\tilde{G}_T$, in Equation 3.48, and thus neglecting the remaining "coupling-correction" terms in 3.49: the plant dynamic mass matrix, G_{P2}, and the RWA dynamic mass matrix, G_{D2}.

In Section 4.3.1, we defined three performance metrics of the structure to be the appendage +z tip displacement and the spring node +z and -y displacements. These performance metrics, obtained by the traditional decoupled analysis method in Equation 2.27, the coupled analysis method in Equation 3.48, and the coupled validation experiment described in Section 4.3, are all plotted for the maximum wheel speed, 2590 RPM, in Figure 5.5. In Figure 5.5(a), the power spectral density and corresponding cumulative RMS of the first performance metric are plotted. (See Section 2.3 for a definition of the cumulative RMS function.) Both the decoupled and coupled analysis methods are overlaid with the experimental data for comparison. Similar plots are presented in Figure 5.5(b) for the second performance metric, and in Figure 5.5(c) for the third performance metric. Since the plots in Figure 5.5 correspond only to the maximum wheel speed, similar results are presented for three other wheel speeds: 2536 RPM in Figure 5.6; 1401 RPM, which would tend to

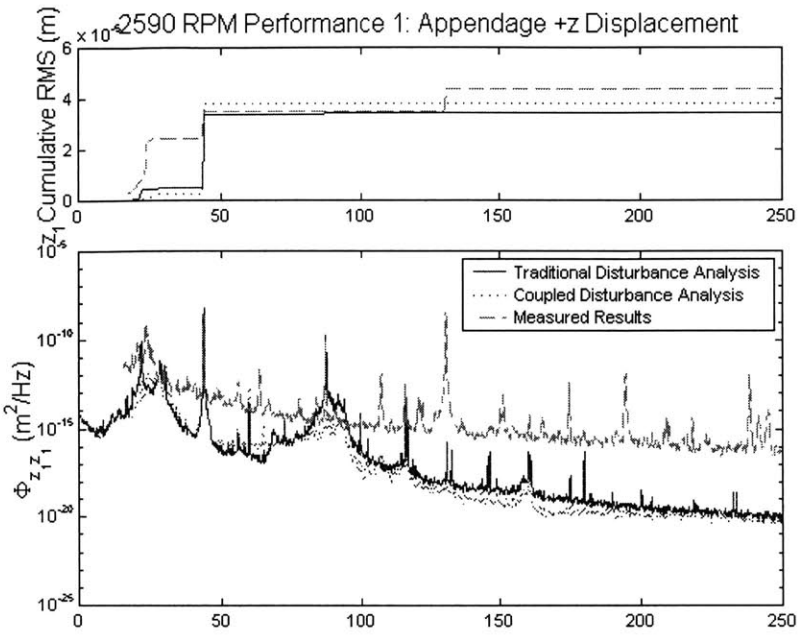

(a) Appendage Tip +z Displacement

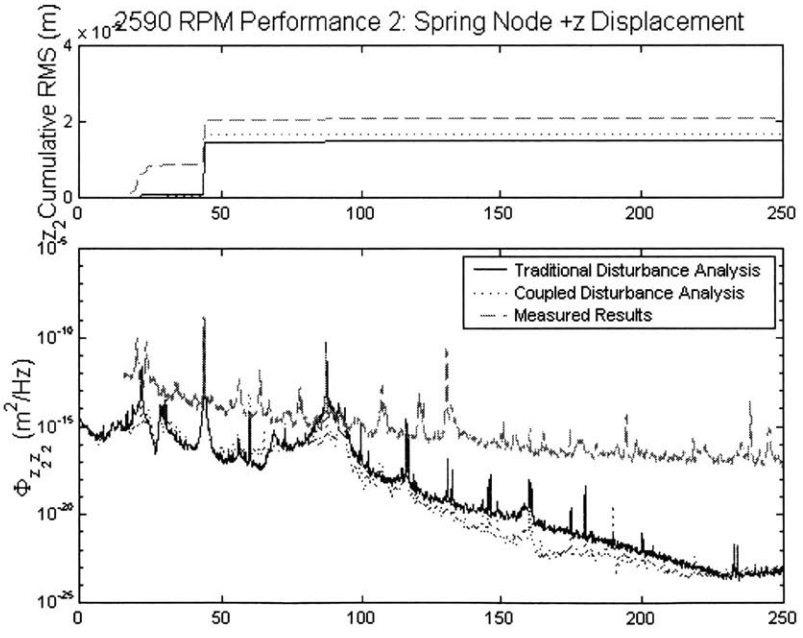

(b) Spring-Node +z Displacement

Figure 5.5 Predicted vs. Measured Performances: 2590 RPM Wheel Speed

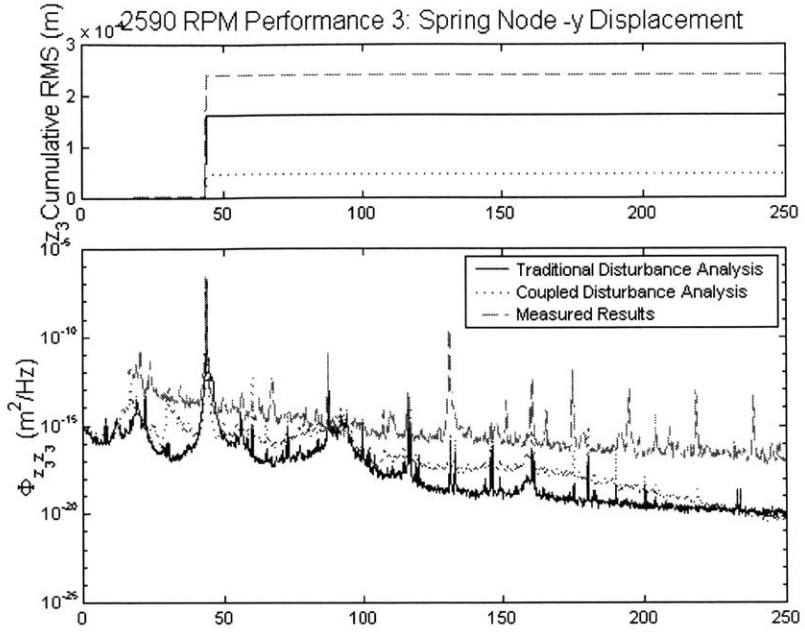

(c) Spring-Node -y Displacement

Figure 5.5 Predicted vs. Measured Performances: 2590 RPM Wheel Speed

excite the ~22 Hz mode of the test structure, in Figure 5.7; and 1022 RPM, one of the lowest practical spin rates of interest, in Figure 5.8.

Based on the coupled analysis theory presented in Chapter 3, we expect the coupled method to generally match the cumulative RMS of the measured performance metrics more closely than the traditional analysis method. Unfortunately, this trend does not appear in the performance data presented here.

Looking more carefully at the cumulative RMS plots in Figures 5.5, 5.6, 5.7, and 5.8, it is difficult to draw any conclusions when comparing the accuracy of the coupled and decoupled analysis methods. At some wheel speeds, both methods underpredict the measured RMS, and at other speeds they both overpredict. At some wheel speeds, the coupled analysis gives a closer prediction, and at other speeds, the decoupled analysis does. It is difficult to find any general trend when comparing the two methods' abilities to accurately predict the system's performance.

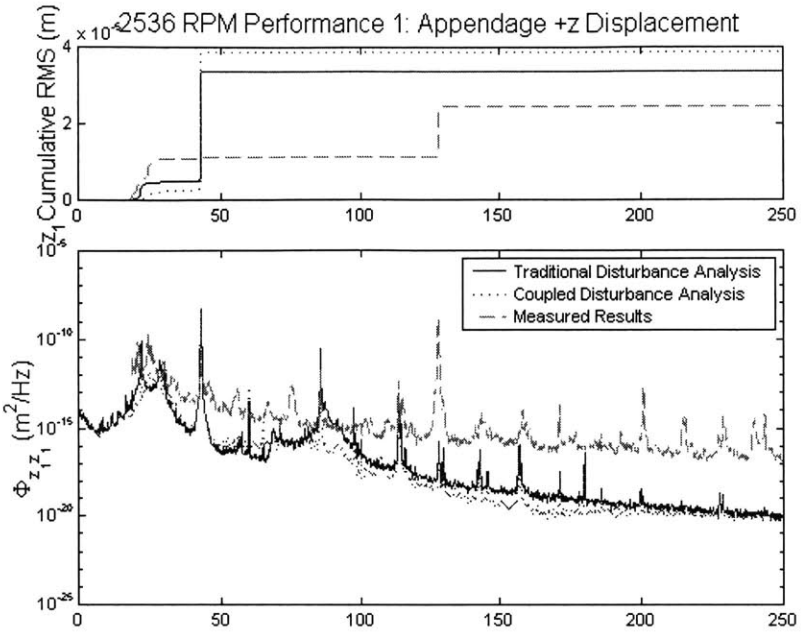

(a) Appendage Tip +z Displacement

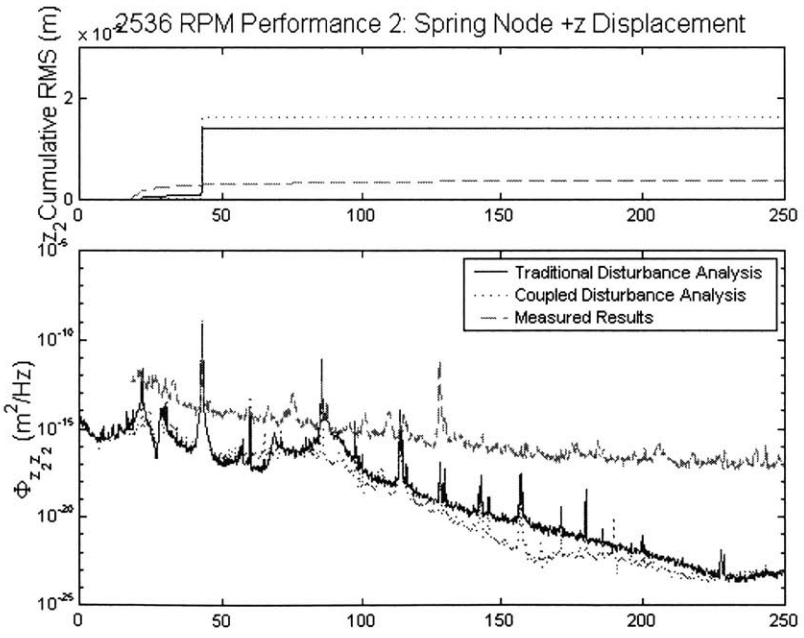

(b) Spring-Node +z Displacement

Figure 5.6 Predicted vs. Measured Performances: 2536 RPM Wheel Speed

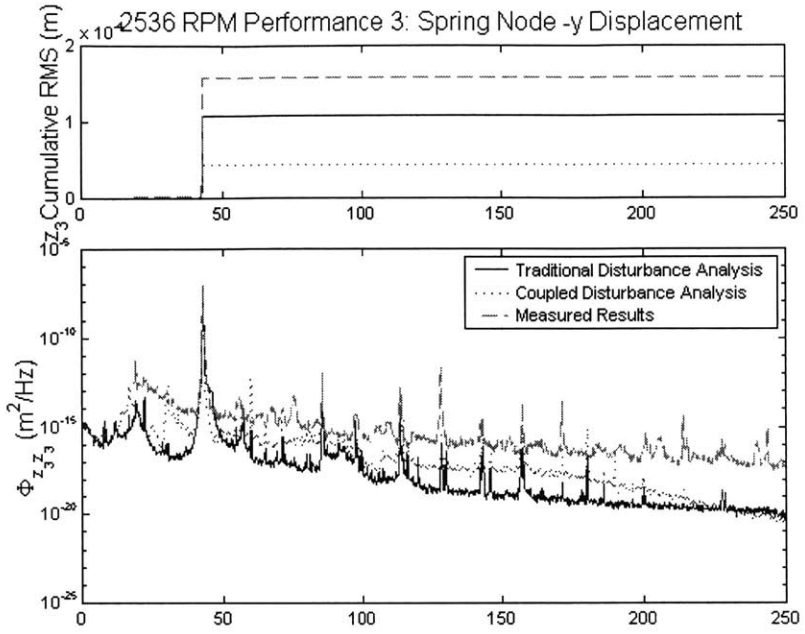

(c) Spring-Node -y Displacement

Figure 5.6 Predicted vs. Measured Performances: 2536 RPM Wheel Speed

Since we have faith in the derivation of the coupled disturbance analysis method presented in Chapter 3, and in its potential improvement over the traditional disturbance analysis methodology discussed in Chapter 2, we must explain the discrepancies in the results presented here. Errors have been largely attributed to three main sources:

- a prohibitively coarse *frequency resolution*.
- accelerometers with an inadequate *signal-to-noise ratio* (SNR).
- the *conversion* process for measured performance metrics *from acceleration PSDs to displacement PSDs* using Equation 3.43.

First consider the *frequency resolution* issue. In Figures 5.5, 5.6, 5.7, and 5.8, we see from the cumulative RMS functions that the total RMS in each case is due almost entirely to a single mode that consistently lies below 50 Hz. (This mode is due to the wheel's primary harmonic disturbance and changes linearly as a function of wheel speed, occurring at a maximum frequency of ~44 Hz, corresponding to the maximum spin rate of 2590 RPM.) Occasionally a secondary mode at ~130 Hz also contributes significantly to the RMS.

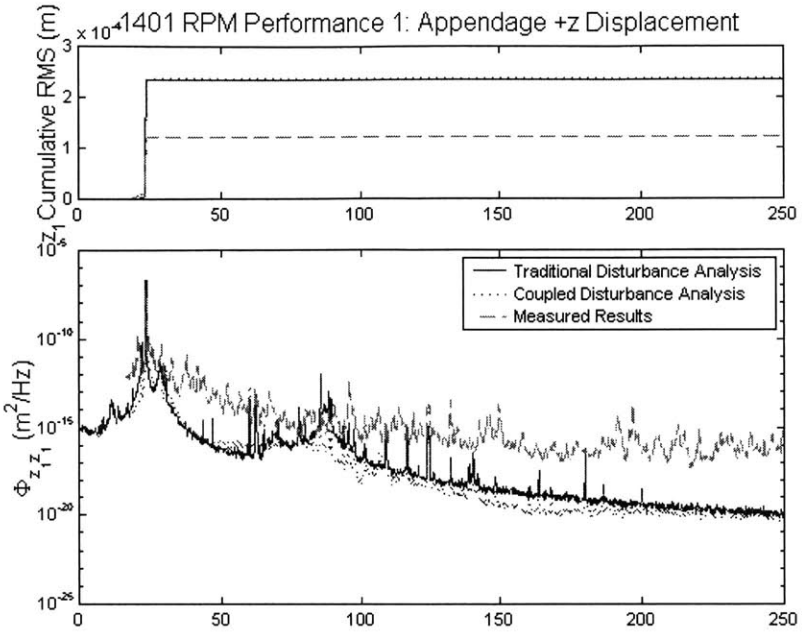

(a) Appendage Tip +z Displacement

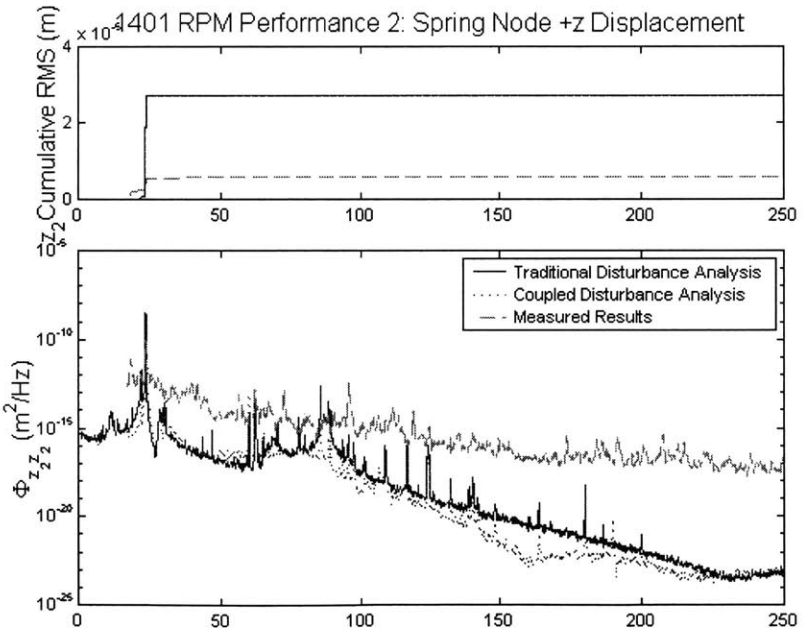

(b) Spring-Node +z Displacement

Figure 5.7 Predicted vs. Measured Performances: 1401 RPM Wheel Speed

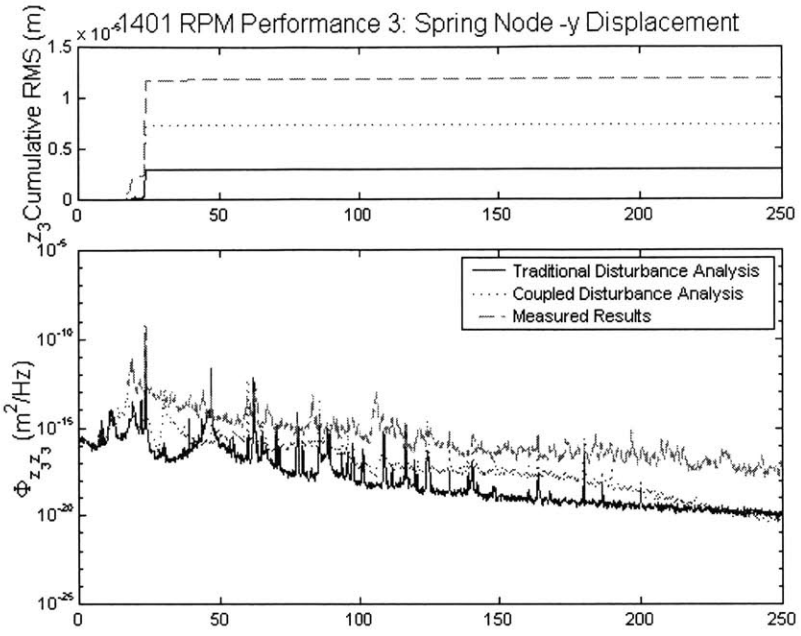

(c) Spring-Node -y Displacement

Figure 5.7 Predicted vs. Measured Performances: 1401 RPM Wheel Speed

Clearly the frequency resolution at these two resonances has a large impact on the quality of the cumulative RMS that is computed by integrating the performance PSD curve, since the resonances essentially define the "step sizes" in the cumulative RMS. However, upon "zooming into" any of the performance PSD plots shown here, one can see that the frequency resolution is quite poor, with resonant peaks that appear digitized and unsmooth and likely do not capture the true resonant maxima. A close-up view of the first performance metric at 2590 RPM, magnified at the ~44 Hz resonance as shown in Figure 5.9, demonstrates that the frequency resolution used here may indeed be too coarse to accurately integrate the performance PSD, yielding an unreliable RMS value.

All of the transfer functions used in the coupled disturbance analysis equations, 3.48 and 3.49, were measured (for the RWA) or produced from a finite element model (for the test structure) with a 250 Hz bandwidth and a ~0.12 Hz frequency resolution. Hence the performances computed using Equation 3.48 have the same frequency resolution, which

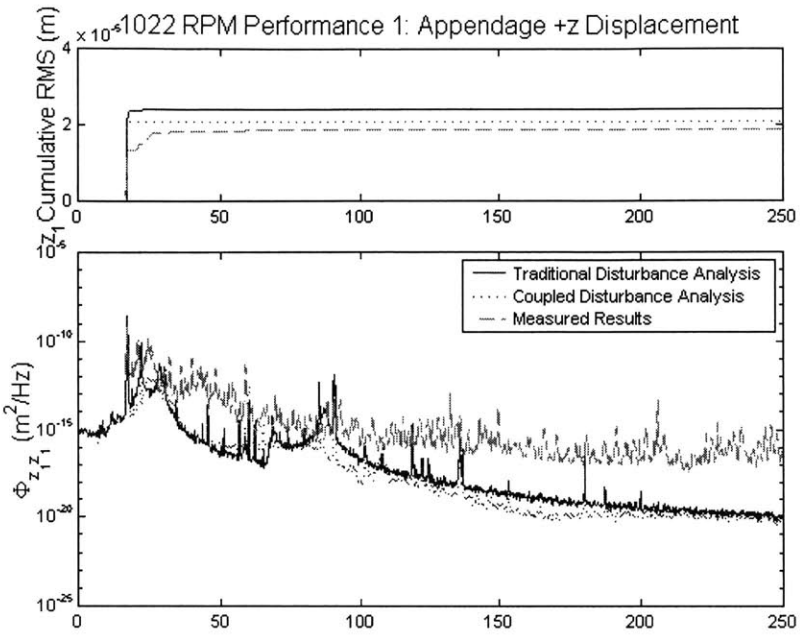

(a) Appendage Tip +z Displacement

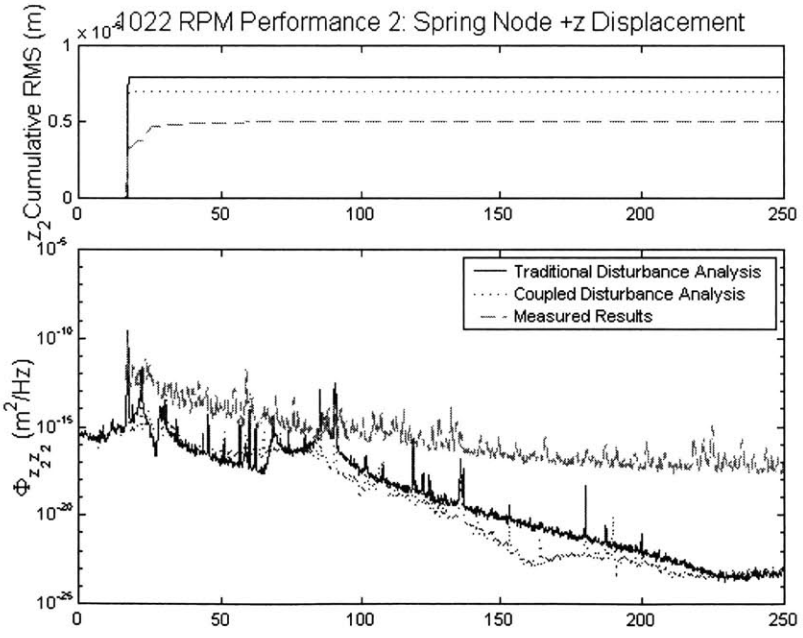

(b) Spring-Node +z Displacement

Figure 5.8 Predicted vs. Measured Performances: 1022 RPM Wheel Speed

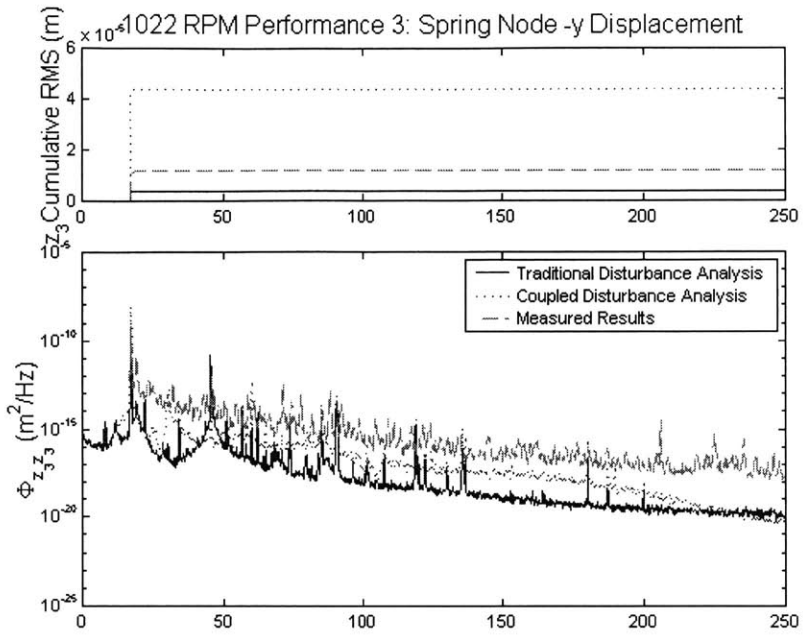

(c) Spring-Node -y Displacement

Figure 5.8 Predicted vs. Measured Performances: 1022 RPM Wheel Speed

proves too coarse for our purposes. Now knowing that the frequency range of interest is much smaller than 250 Hz (with the highest influential resonance occurring at ~130 Hz), we could reperform all of these tests at a lower sampling frequency, concentrating the excitation energy to a smaller bandwidth, and thus refining the frequency resolution, giving us more confidence in the quality of the resonant peaks and the computed RMS values.

Next consider the *accelerometer SNR* issue. In Figure 5.10, the PSD of the third performance metric with the wheel spinning at 1401 RPM is overlaid with the same metric at zero RPM; in other words, it is overlaid with the metric resulting from an accelerometer measuring only noise. We see that the accelerometer noise floor lies significantly (~1-2 orders of magnitude!) above the "backbone" of the performances predicted by the decoupled and coupled methods. Further, the integrated accelerometer noise is significant enough to cause a non-zero cumulative RMS. Figure 5.10 demonstrates for the third performance metric that the RMS error due to noise integration can be over 25% of the total

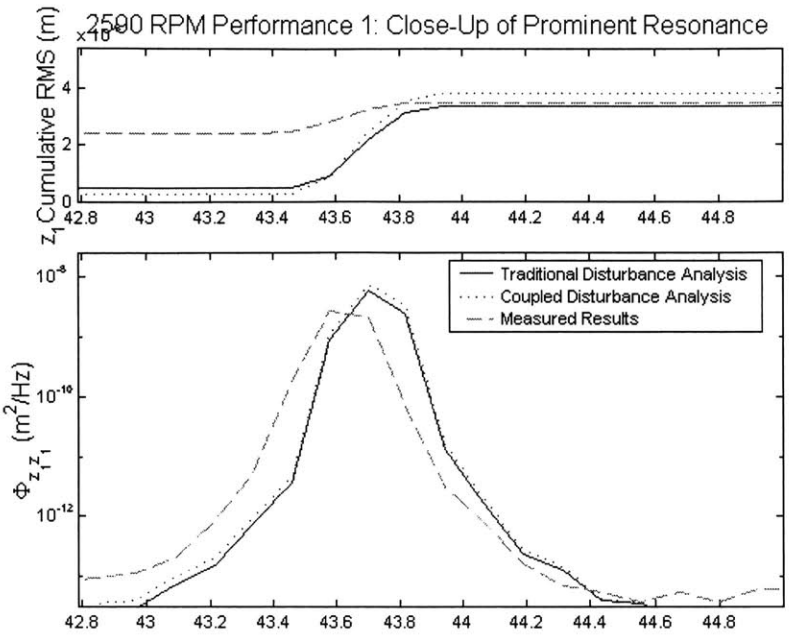

Figure 5.9 "Zoomed in" View of the ~44 Hz Resonance at 2590 RPM, Demonstrating a Poor Frequency Resolution.

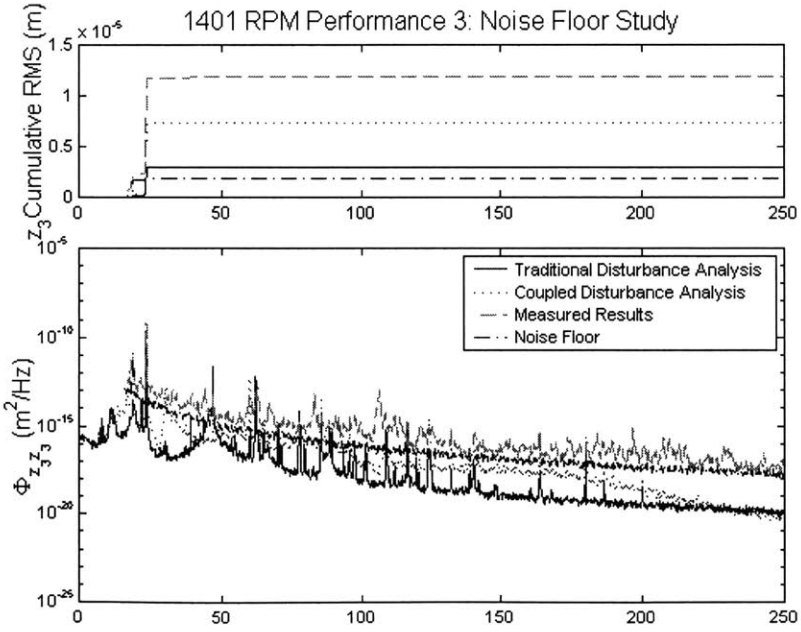

Figure 5.10 1401 RPM Performance Metric 3 vs. Accelerometer Noise Floor

RMS value at 1401 RPM. With this poor SNR, we cannot have great confidence in our accelerometer measurements and must be weary of measuring and integrating (via the cumulative RMS) accelerometer noise. Hence the results may be improved by exchanging the current accelerometers for sensors with a lower noise floor relative to the signal of interest.

Also notice that some of the cumulative RMS plots of the measured performances display gradual gains with increasing frequency, rather than the distinct "steps" at resonant frequencies that usually indicate the contribution of distinct vibrational modes to the RMS. This is further evidence of the integration of noise due to the low SNR of the accelerometer data, resulting from the use of accelerometers that are not sensitive enough to capture the small-magnitude structural vibrations induced here.

The RMS error demonstrated in Figure 5.10 can also be attributed to the third error source, the *acceleration-to-displacement PSD conversion*. The difficulty in this conversion lies in the division by frequency of acceleration PSDs to yield displacement PSDs. We see from Equation 3.43 that for very low frequencies, the displacement PSDs become infinite!

Although the accelerometers used in these experiments do not measure DC, they are accurate to as low as ~1 Hz. Theoretically this implies that the displacement PSDs obtained from Equation 3.43 should be accurate to as low as ~1 Hz. However, conversion of the acceleration PSDs obtained in these experiments leads to unusually large displacement PSDs at frequencies *above* 1 Hz, even as high as ~10 Hz. This introduces the dilemma of choosing a lower frequency limit for the integration of the displacement PSD to obtain its cumulative RMS using Equation 2.25. It is a subjective trade between, on one hand, beginning the integration at a sufficiently low frequency to capture all the dynamics of interest, but accumulating the "conversion noise" at low frequencies, thus causing the cumulative RMS to be erroneously large, and, on the other hand, beginning the integration at a higher frequency in order to eliminate integrating the "conversion noise," but possibly failing to capture some of the lower frequency dynamics. Because of the subjectivity of

choosing an appropriate lower integration limit, one cannot have firm confidence in an RMS value obtained by integrating a displacement PSD derived from an acceleration PSD via Equation 3.43, unless the dynamics of interest are well beyond the low-frequency range of the "conversion noise." This integration error and the uncertainty that arises from the acceleration-to-displacement PSD conversion can be avoided in the future by using displacement sensors to measure performance, rather than accelerometers.

In each of the performance plots presented in Figures 5.5, 5.6, 5.7, and 5.8, the decoupled and coupled analytical performance predictions are shown in their original form, as displacement PSDs, but the *measured* performance PSDs are obtained by converting acceleration PSDs to displacement PSDs using Equation 3.43. For this reason, each *measured* PSD is truncated at a lower limit immediately below its first major contributing mode, in order to minimize conversion error while still capturing the influential dynamics. In most cases, this lower limit was found to be between 15 and 20 Hz. Attempts to decrease this lower limit confirmed an increase in noise accumulated by the cumulative RMS when integrating over low-frequency values of the displacement PSDs.

5.4 Summary

In this chapter, experimental results were presented for hard-mounted and coupled RWA disturbance tests, free-free RWA dynamic mass tests, and coupled structure-RWA tests. Test results and FEM-based transfer functions were then combined to predict the system performance from decoupled and coupled analyses, using the coupled experimental results for comparison.

In Section 5.1, disturbance spectra from a representative reaction wheel, both in hard-mounted and structurally-coupled configurations, were presented. These spectra prove to be significantly different from one another, since the hard-mounted spectra display severe amplifications where the disturbance harmonics interfere with flexible wheel modes, and the coupled spectra display similar amplifications where the harmonics interfere with the test structure's flexible modes. Further, the hard-mounted spectra generally contain

higher frequency content and higher non-amplified harmonic magnitudes, as a result of the "overtest" condition that occurs in the hard-mounted configuration. Finally, the symmetry that generally occurs in hard-mounted radial force and torque spectra was lost in the coupled spectra, due to the asymmetry of the mounting structure.

In Section 5.2, some dynamic mass data obtained from the free-free tests on the RWA were presented. The fundamental frequency of the lever arm that was appended to the RWA in these tests was found to be ~53 Hz, and it was determined that this mode does not corrupt the data.

Finally, in Section 5.3, the results of the decoupled disturbance analysis, the coupled disturbance analysis, and the coupled laboratory experiment were all presented. The power spectral densities of the three performance metrics obtained from the two analyses and the experiment, along with their cumulative RMS functions, were plotted for a selection of wheel speeds.

While the performance plots did not confirm the benefits of the proposed coupled method over the traditional decoupled disturbance analysis method, errors have been attributed to three main sources:

- a prohibitively coarse *frequency resolution.*
- accelerometers with an inadequate *signal-to-noise ratio* (SNR).
- the *conversion* process for measured performance metrics *from acceleration PSDs to displacement PSDs* using Equation 3.43.

Recommendations for more accurate results in the future include:

- use of a lower excitation bandwidth, resulting in a refined frequency resolution and higher-fidelity cumulative RMS calculations.
- use of sensors with an improved SNR, or conversely, a system with larger magnitude excitations so that performances can be accurately measured using the given sensors.
- use of displacement sensors, rather than accelerometers. If only acceleration sensors are available, one must ensure that the dynamics of interest occur

above the low-frequency range of acceleration-to-displacement PSD conversion noise.

Chapter 6

CONCLUSIONS

6.1 Summary

The future of space telescopes lies with large, lightweight, flexible structures whose dynamic characteristics are a great factor in the telescopes' abilities to achieve scientific goals. The primary vibrational disturbance source aboard most space telescopes is the reaction wheel assembly (RWA) used for attitude control.

This thesis reviews the most commonly used method of frequency-domain disturbance analysis of flexible structures with disturbance-inducing RWAs, investigates the simplifying assumptions made in this type of analysis and the potential errors they may induce, and proposes a new *coupled* disturbance analysis method for application to flexible spacecraft-RWA systems.

In Chapter 2, the nature of RWA disturbances and the typical hard-mounted testing method of RWAs is introduced. RWA disturbances are composed of a primary harmonic and sub- and superharmonics of the wheel's spin rate. The dominant flexible modes of a reaction wheel are the axial translation, radial translation, and radial rocking modes. The disturbances are usually measured in six-axes, as three forces and three moments, in a hard-mounted configuration.

Useful techniques in data processing in the time and frequency domains are then presented, including the Finite Fourier Transform, the Power Spectral Density, and the Cumulative RMS. Most importantly, the process of converting hard-mounted RWA disturbance data to a 6×6 spectral density matrix, $\Phi_{FF}(\omega)$, is explained. A popular method of spacecraft-RWA frequency domain disturbance analysis, which combines the disturbance matrix $\Phi_{FF}(\omega)$ with a structural transfer function, $G_{ZF}(\omega)$, obtained from a finite element model of the structure to predict the resulting performance metrics, is then reviewed, along with a discussion on the limitations of this method.

An amended disturbance analysis method, which accounts for the structural dynamic coupling between a spacecraft and its RWA, is presented in Chapter 3. First a sample problem is used to motivate the coupled disturbance analysis method for flexible spacecraft-RWA systems. This spring-mass problem demonstrates that the traditional decoupled disturbance analysis method, when applied to a two-DOF coupled system, is only an approximation of a coupled disturbance analysis, but that this approximation may be accurate if the spacecraft mass is significantly larger than the RWA mass. The limitation is that the study is performed on a simple, two-DOF system, and the results can not necessarily be extended to complex, multi-DOF systems.

The theory for a coupled disturbance analysis technique is then presented. The suggested method requires both an RWA for experimental testing and a finite element model of the spacecraft, as in the traditional method; however, it improves upon the traditional method by including the RWA's dynamic mass, G_{D2}, as a coupling correction term in the analysis. In summary, a coupled disturbance analysis involves the following steps:

- Determine the spacecraft transfer functions G_{P1} and G_{P2} from the spacecraft finite element model (Section 3.3.3).
- Determine the RWA dynamic mass transfer function, G_{D2}, from free-free testing of the RWA and Equations 3.56, 3.58, and 3.60.
- Determine the RWA disturbance spectra $\Phi_{FF}\big|_{W}$ from hard-mounted testing of the RWA (Section 2.2.1).

- Calculate the coupled spacecraft-RWA performance Φ_{ZZ} by substituting G_{P1}, G_{P2}, G_{D2}, and $\Phi_{FF}|_W$ into Equations 3.48 and 3.49.

Chapter 4 describes three different types of laboratory experiments performed to validate this coupled disturbance analysis method in the MIT Space Systems Laboratory:

1. RWA hard-mounted tests, which yield a 6×6 spectral density matrix, $\Phi_{FF}|_W$, for each wheel speed.
2. RWA free-free dynamic mass tests, which yield a 6×6 coupling correction matrix, G_{D2}, and
3. coupled validation tests, which yield the three performance metrics of a representative test structure for each wheel speed.

In Chapter 5, experimental results are presented for hard-mounted and coupled RWA disturbance tests (test 1), free-free RWA dynamic mass tests (test 2), and coupled structure-RWA tests (test 3).

First in Section 5.1, the disturbance spectra from a representative reaction wheel, both in hard-mounted and structurally-coupled configurations, are presented. While test 1 requires only hard-mounted RWA disturbance tests, coupled disturbance tests with the RWA mounted to a test structure are also performed, and the results prove quite different. The hard-mounted spectra display severe amplifications where the disturbance harmonics interfere with flexible wheel modes, and the coupled spectra display similar amplifications where the harmonics interfere with the test structure's flexible modes. Further, the hard-mounted spectra generally contain higher frequency content and higher non-amplified harmonic magnitudes, as a result of the "overtest" condition that occurs in the hard-mounted configuration. Finally, the symmetry that generally occurs in hard-mounted radial force and torque spectra was lost in the coupled spectra, due to the asymmetry of the mounting structure.

In Section 5.2, the dynamic mass data obtained from test 2, the free-free RWA test, are presented.

In Section 5.3, the results of the decoupled disturbance analysis, the coupled disturbance analysis, and the coupled laboratory experiment are all presented. The traditional *decoupled* disturbance analysis applies test 1 results to the structural finite element model to predict its performance. The proposed *coupled* disturbance analysis appends the test 2 results to those of test 1 in order to predict the structure's performance. Finally, the measured results from test 3 are presented and compared to the decoupled and coupled disturbance analyses in order to assess which better predicts the true coupled performance. The analytical and measured performances are plotted in spectral density and cumulative RMS form for a variety of wheel speeds.

While the performance plots do not confirm the expected benefits of the proposed coupled method over the traditional decoupled disturbance analysis method, errors are attributed to three main sources:

- a prohibitively coarse frequency resolution.
- accelerometers with an inadequate signal-to-noise ratio (SNR).
- the conversion process for measured performance metrics from acceleration PSDs to displacement PSDs.

6.2 Recommendations for Future Work

The theory for a coupled disturbance analysis method was presented in this thesis, but the laboratory experiments performed to validate this method did not successfully demonstrate the benefits of the coupled analysis method over the traditional, decoupled method. In order to successfully validate the proposed method, one should reperform the experiments and analysis attempted in this thesis, while eliminating the sources of error outlined above. Recommendations for obtaining more accurate results include:

- use of a lower excitation bandwidth, yielding a refined frequency resolution and higher-fidelity cumulative RMS calculations.
- use of sensors with an improved SNR, or conversely, a system with larger magnitude excitations so that performances can be accurately measured using the given sensors.

- use of displacement sensors, rather than accelerometers. If only acceleration sensors are available, one must ensure that the dynamics of interest occur above the low-frequency range of acceleration-to-displacement PSD conversion noise.

Once the coupled analysis method has been successfully validated, the work may be extended to a *variable-mass system*. Recall the conclusion drawn from the two-DOF sample problem presented in Section 3.1: the traditional decoupled disturbance analysis method, when applied to a two-DOF coupled system, may be an accurate approximation of the coupled system if the spacecraft mass is significantly larger than the RWA mass. We noted that this conclusion is valid for our simple, two-DOF system, but that the results can not necessarily be extended to complex, multi-DOF systems. Hence the next logical step after validating the coupled disturbance analysis method would be to investigate its dependence on the mass ratio of the spacecraft and RWA.

If we rotate the two-DOF system on its side, as shown in Figure 6.1(a), it suggests a new multi-DOF test structure that could be used to investigate this problem. Figure 6.1(b) shows a new test structure designed and built in the Space Systems Laboratory at MIT for the purposes of these proposed structure-RWA coupled tests, as well as for a separate "isoperformance" study, which attempts to trade parameters of the disturbance and plant in search of equal performances. The structure has two primary stages: an upper stage, which provides a mounting location for the RWA, and a lower stage, which resembles a plant with a variable mass. The weight bed on the bottom stage is capable of carrying weights ranging from zero lb. to 200 lb. Since the RWA weighs ~19 lb., this results in a structure-to-RWA mass ratio variable between roughly one and ten.

The following steps are recommended to perform a mass-dependent investigation of the coupled disturbance analysis method:

- Select a set of desired performance metrics for this structure.
- Create a finite element model (FEM) of the structure.

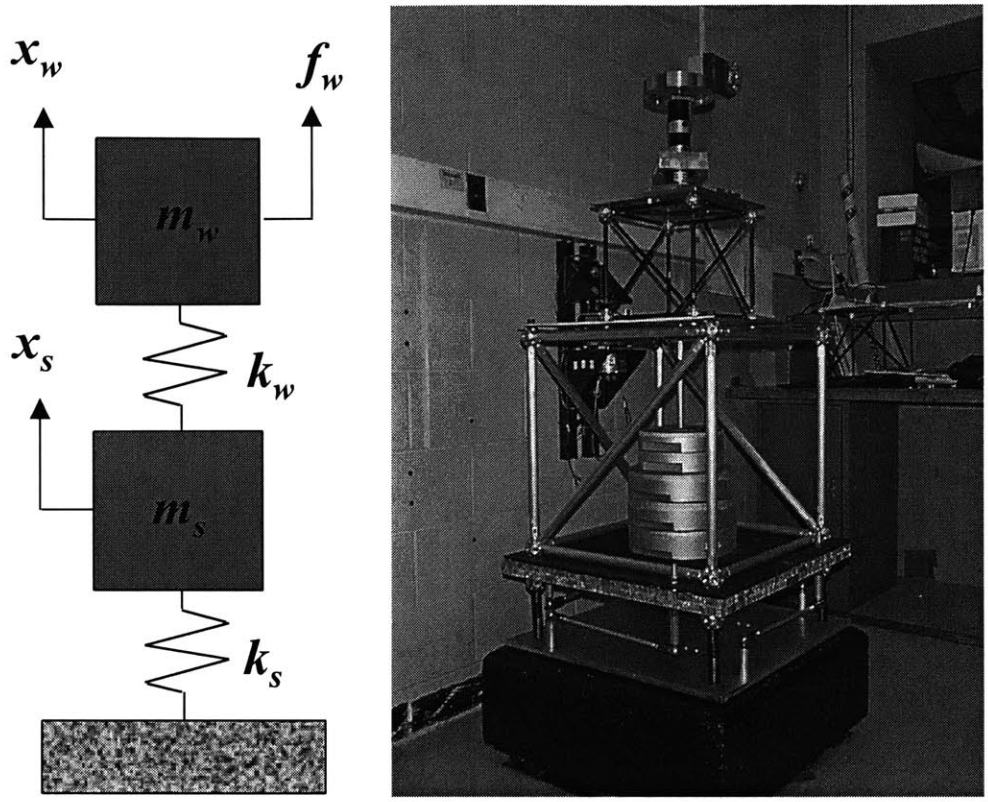

Figure 6.1 (a) Rotated Two-DOF Sample System (b) New Mass-Variable Test Structure for Structure-RWA Coupled Disturbance Analyses

- Validate the FEM by performing system identification tests, comparing the measured and FEM-predicted performance metrics, and updating the model to reflect the data.
- Obtain the plant transfer functions G_{P1} and G_{P2} from the FEM, as was done for the test structure used in this thesis.
- Perform both decoupled and coupled disturbance analyses, and obtain measured performances of the coupled system for various wheel speeds, as was done for the test structure used in this thesis.
- Reperform both analyses and the experimental measurements for a variety of structure-to-RWA mass ratios, and attempt to draw analogous conclusions to those drawn for the two-DOF sample problem. It will be interesting to find whether a higher mass ratio yields a better decoupled approximation of the coupled system, as found in the sample problem.

REFERENCES

[Bathe, 1996] Bathe, K.J., *Finite Element Procedures*, Prentice-Hall, Inc., 1996.

[Bialke, 1997] Bialke, B., "A Compilation of Reaction Wheel Induced Spacecraft Disturbances", *20th Annual AAS Guidance and Control Conference*, February 1997. AAS Paper 97-038.

[Chen, 1992] Chen, G.S. and B.J. Lurie, "Active Member Bridge Feedback Control for Damping Augmentation", *Journal of Guidance, Control, and Dynamics* **15**, pp. 1155-1160, 1992.

[Craig, 1981] Craig, R., Jr., *Structural Dynamics: An Introduction to Computer Methods*, John Wiley & Sons, Inc., 1981.

[Franklin, 1994] Franklin, G.F., J.D. Powell, and A. Emami-Naeini, *Feedback Control of Dynamic Systems*, Addison-Wesley Publishing Company, Inc., 1994.

[Glaese, 1997] Glaese, R.M., *Impedance Matching for Structural-Acoustic Control*, Ph.D. thesis, Massachusetts Institute of Technology, April 1997.

[GSFC] Goddard Space Flight Center, *Next Generation Space Telescope Home Page*, URL <http://ngst.gsfc.nasa.gov>. Accessed January 30, 2001.

[Gutierrez, 1999] Gutierrez, H.L., *Performance Assessment and Enhancement of Precision Controlled Structures During Conceptual Design*, Ph.D. thesis, Massachusetts Institute of Technology, February 1999.

[Hagood, 1990] Hagood, N.W. and E.F. Crawley, "Approximate Frequency Domain Analysis for Linear Damped Space Structures," *AIAA Journal* **28**, pp. 1953-1961, 1990.

[Ithaco] Ithaco Space Systems, *Torqwheel*, URL <http://www.ithaco.com/T-Wheel.html>. Accessed January 30, 2001.

[Kreyszig, 1993] Kreyszig, E., *Advanced Engineering Mathematics*, John Wiley & Sons, Inc., 1993.

[JPL] Jet Propulsion Laboratory, *NASA's Origins Program*, URL <http://origins.jpl.nasa.gov>. Accessed January 30, 2001.

[JPL] Jet Propulsion Laboratory, *Space Interferometry Mission*, URL <http://sim.jpl.nasa.gov>. Accessed January 30, 2001.

[Masterson, 1999] Masterson, R.A., *Development and Validation of Empirical and Analytical Reaction Wheel Disturbance Models*, Master's thesis, Massachusetts Institute of Technology, June 1999.

[NASA] Nasa Headquarters, *The NASA Origins Program*, URL <*http://www.hq.nasa.gov/office/pao/facts/HTML/FS-020-HQ.html*>. Accessed February 8, 2001.

[Neat, 1998] Neat, G.W., J.W. Melody, and B.J. Lurie, "Vibration Attenuation Approach for Spaceborne Optical Interferometers", *IEEE Transactions on Control Systems Technology* **6**, November 1998.

[Scharton, 1999] Scharton, T.D., "Equivalent Source Models of Ithaco Reaction Wheel", *Unpublished Technical Document*, 27 April 1995.

[Scharton, 1995] Scharton, T.D., "Vibration-Test Force Limits Derived from Frequency-Shift Method", *Journal of Spacecraft and Rockets* **32**, pp. 312-316, 1995.

[Stearns, 1990] Stearns, S.D., and D.R. Hush, *Digital Signal Analysis*, Prentice-Hall, 1990.

[STSCI] Space Telescope Science Institute, *Space Telescope Science Institute Homepage*, URL <*http://www.stsci.edu*>. Accessed February 8, 2001.

[Strang, 1986] Strang, G., *Introduction to Applied Mathematics*, Wellesley-Cambridge Press, 1986.

[Thomson, 1993] Thomson, W.T., *Theory of Vibrations with Applications*, Prentice-Hall, Inc., 1993.

[Uebelhart, 2001] Uebelhart, S.A., *Conditioning, Reduction, and Disturbance Analysis of Large Order Integrated Models for Space-Based Telescopes*, Master's thesis, Massachusetts Institute of Technology, February 2001.

[Wirsching, 1995] Wirsching, P.H., T.L. Paez, and H. Ortiz, *Random Vibrations: Theory and Practice*, John Wiley & Sons, Inc., 1995.